

Parity-dependent double degeneracy and spectral statistics in the projected dice lattice

Koushik Swaminathan¹, Anouar Moustaj¹, Jose L. Lado¹, and Sebastiano Peotta^{1,*}

¹Department of Applied Physics, Aalto University, FI-00076 Aalto, Finland

We investigate the spectral statistics of an interacting fermionic system derived by projecting the Hubbard interaction onto the two lowest-energy, degenerate flat bands of the dice lattice subjected to a π -flux. Surprisingly, the distributions of level spacings and gap ratios correspond to distinct Gaussian ensembles, depending on the parity of the particle number. For an even number of particles, the spectra conform to the Gaussian Orthogonal Ensemble, as expected for a time-reversal-symmetric Hamiltonian. In stark contrast, the odd-parity sector exhibits exact double degeneracy of all eigenstates even after resolving all known symmetries, and the Gaussian Unitary Ensemble accurately describes the spacing distribution between these doublets. The simultaneous emergence of two different random-matrix ensembles within a single physical system constitutes an unprecedented finding, opening new avenues for both random matrix theory and flat-band physics.

Flat electronic bands are a flexible building block for collective states of matter. In particular, in moiré materials, a slight twist between atomic layers produces nearly dispersionless bands and dramatically amplifies interaction effects [1–3]. These flat-band platforms host a variety of correlated phases, such as unconventional superconductivity [1, 4–7] and fractional quantum Hall states [8–11].

A common strategy for tackling the strongly interacting problem posed by lattice models with flat bands is to project the interaction term onto the flat-band subspace, thereby significantly reducing the Hilbert-space dimension [12–16]. The trade-off is that the resulting projected Hamiltonian consists of a large number of nonlocal terms, which hampers both analytical treatment and large-scale numerics [16]. Moreover, purely quartic Hamiltonians obtained via flat-band projection often exhibit emergent symmetries, quantum scars, and Hilbert-space fragmentation [17–20], with profound effects on transport and many-body dynamics.

The dice lattice [13, 21, 22] (Fig. 1(a)) offers a highly tractable platform for investigating these effects. Its flat bands support compactly localized Wannier functions, which allow the projected Hamiltonian to be written as a finite collection of short-range terms. This convenient structure has enabled detailed studies of the lattice’s many-body physics, including prior reports of quasiparticle localization that may arise from emergent local integrals of motion (LIOMs) [20]. Here, we examine the spectral statistics, specifically, the level spacing and gap ratios distributions, to resolve the open question of whether LIOMs are present in this system.

In generic nonintegrable systems, level spacing and gap ratio distributions follow the Gaussian orthogonal, unitary or symplectic ensembles (GOE/GUE/GSE) of random matrix theory (RMT) [23–25], while systematic deviations signal hidden symmetries, integrability, or fragmentation of the Hilbert space [26–28]. In particular,

higher-order (k -nearest-neighbor, k NN) spectral statistics have recently emerged as sensitive probes of multi-block spectra and hidden symmetries [29–31].

In this work, we analyze the spectral statistics of the Hamiltonian obtained by restricting a Hubbard interaction to the two lowest degenerate flat bands of the dice lattice threaded by a π -flux. Exact diagonalization in symmetry-resolved sectors reveals a surprising parity dichotomy. For even total particle number, the spectrum is nondegenerate (see Fig. 1(b)) and the spectral statistics at any order k correspond to the superposition of m independent matrix blocks in the GOE. The number of blocks m changes with system size, suggesting the presence of an extensive number of LIOMs, which would explain the nonergodic dynamics observed previously [20]. Instead, for odd parity, the spectral statistics display entirely unexpected features. The full spectrum is doubly degenerate even after resolving all known symmetries, such as spin rotation (see Fig. 1(c)), and for all accessible cluster sizes, the spacing distribution of the doublets ($k = 2$ and 4 order statistics) matches that of the GUE.

Our work highlights the usefulness of higher-order spectral statistics and, most importantly, reveals an unprecedented phenomenon, the coexistence of different random-matrix ensembles (GOE and GUE) in the same physical system, which is a minimal and paradigmatic lattice model with flat bands. More surprisingly, the switch from one ensemble to the other occurs simply by removing or adding a single particle. This suggests the existence of a new class of Hamiltonians that defy the expectations from RMT.

Model and symmetries—The Wannier functions w_{nl} of the two lowest flat bands of the dice lattice with π -flux can be taken to be compactly localized [13, 17, 21, 22, 33], as seen in Fig. 1(a). Consequently, the projection yields an effective interaction with a finite number of nearest-neighbor terms acting within the flat-band subspace, which we parametrize as

$$\hat{\mathcal{H}}_{\lambda_2, \lambda_3} = \hat{\mathcal{H}}_{\text{tri.}} + \lambda_2 \hat{\mathcal{H}}_{\text{kag.}} + \lambda_3 \hat{\mathcal{H}}_{\text{tri.-kag.}} \quad (1)$$

The first term $\hat{\mathcal{H}}_{\text{tri.}}$ describes the motion of on-site pairs

* sebastiano.peotta.work@protonmail.com

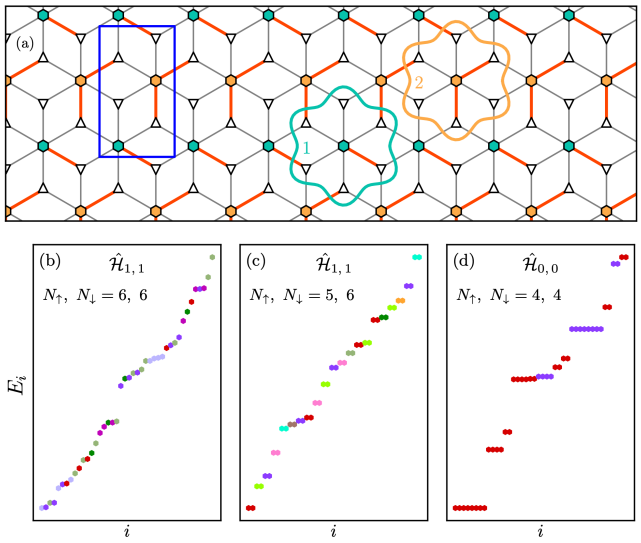


FIG. 1. (a) Schematic of the dice lattice. The box is the magnetic unit cell comprising six lattice sites, while the thin black (thick red) bonds represent positive (negative) hopping amplitudes $t > 0$ ($-t < 0$). Wannier functions w_{n1} ($n = 1, 2$) of the two lowest flat bands are also shown. (b)-(d): Interior eigenvalues of $\hat{\mathcal{H}}_{\lambda_2, \lambda_3}$ (1) for system size $N_x, N_y = 3, 2$, momentum $\mathbf{k} = 0$, and particle numbers N_\uparrow, N_\downarrow shown in each panel. Different colors indicate different pairs (S, B) of total spin and pseudospin quantum numbers. For even particle numbers (b), the eigenvalues E_i are nondegenerate. For odd particle numbers (c), the spectrum consists of degenerate doublets. When $\lambda_2 = \lambda_3 = 0$ (d), highly degenerate multiplets appear due to known LIOMs [20, 32].

and the exchange interaction between spins, $\hat{\mathcal{H}}_{\text{kag}}$, controls the dynamics of pairs delocalized on two neighboring Wannier functions (bond singlets), which move in an effective kagome lattice, and $\hat{\mathcal{H}}_{\text{tri-kag}}$ is a term converting on-site into bond singlets and viceversa. The projected Hamiltonian of the dice lattice is realized for $\lambda_2 = \lambda_3 = 1$. The explicit forms of all terms are given in Ref. [20] and in the Supplemental Material [32].

The Hamiltonian Eq. (1) possesses many symmetries that should be resolved when analyzing its spectral statistics. Under periodic boundary conditions, $\hat{\mathcal{H}}_{\lambda_2, \lambda_3}$ commutes with the translation operators of a rectangular Bravais lattice. Thus, the eigenstates are labeled by the crystal momentum $\mathbf{k} = (k_x, k_y)$, with $0 \leq k_\mu < N_\mu$ on a system composed of $N_x \times N_y$ unit cells. In the presence of the π -flux, point-group symmetries such as reflections and two-fold rotations are dressed by gauge transformations. Therefore, their respective quantum numbers cannot be resolved simultaneously with momentum \mathbf{k} [32].

The Hamiltonian possesses also full SU(2) spin symmetry since it commutes with the spin ladder operator $\hat{S}^+ = \sum_{n1} \hat{d}_{n1\uparrow}^\dagger \hat{d}_{n1\downarrow}$ and the total spin operator $\hat{S}^2 = (S^z)^2 + \frac{1}{2}(\hat{S}^+ \hat{S}^- + \hat{S}^- \hat{S}^+)$, where $\hat{d}_{n1\sigma}$ is the fermionic annihilation operator corresponding to Wannier function

w_{n1} and $\sigma = \uparrow, \downarrow$. When $N_\uparrow = N_\downarrow$, there is an additional spin-flip symmetry, $S^z \rightarrow -S^z$. Even (odd) states under spin flip are labeled by $f = +(-)$. Moreover, for $\lambda = \lambda_2 = \lambda_3$ one has the relation $[\hat{\mathcal{H}}_{\lambda, \lambda}, \hat{B}^+] = -E_p \hat{B}^+$ (called a spectrum generating algebra [28, 34, 35]), where the operator $\hat{B}^+ = \sum_{n1} \hat{d}_{n1\uparrow}^\dagger \hat{d}_{n1\downarrow}^\dagger$ creates an on-site pair in a zero momentum state. Even for nonzero binding energy E_p , this implies that the eigenstates can be labeled by the eigenvalues of the form $B(B+1)$ of the total *pseudospin* operator $\hat{B}^2 = (\hat{B}^z)^2 + \frac{1}{2}(\hat{B}^+ \hat{B}^- + \hat{B}^- \hat{B}^+)$ [15]. Numerically, the basis of a sector with given particle numbers N_\uparrow and N_\downarrow , momentum \mathbf{k} , and (if applicable) spin-flip parity f is constructed using QuSpin [36, 37], and the spin S and pseudospin B quantum numbers are resolved by diagonalizing $\hat{\mathcal{H}}_{\lambda_2, \lambda_3} + \alpha \hat{S}^2 + \beta \hat{B}^2$ with large α, β [38, 39].

The term $\hat{\mathcal{H}}_{\text{tri}}$ in (1) commutes with an extensive number of LIOMs, namely the total spin operators \hat{S}_{n1}^2 of each Wannier function [20]. Whether these LIOMs are either broken or deformed for nonzero λ_2 and λ_3 is the open question that motivates this work. Finally, it is important to note that the Hamiltonian is time-reversal symmetric since all hopping matrix elements are real.

Spectral statistics—For an ordered spectrum $\{E_n\}$, we define the k NN (k -order) level spacings

$$\tilde{s}_n^k = E_{n+k} - E_n, \quad k = 1, 2, 3, 4. \quad (2)$$

To remove the smooth energy dependence of the density of states, these spacings are unfolded and normalized according to $s_n^k = \tilde{s}_n^k / \langle \tilde{s}^k \rangle_{\text{local}}$, such that $\langle s^k \rangle_{\text{local}} \simeq 1$ [32, 39, 40]. The resulting distributions $P^k(s)$ are then compared to the universal predictions of RMT. It is natural to consider the second and higher-order level spacings due to the degeneracy observed for odd parity. The distribution of k NN level spacings is also useful to identify independent blocks [29, 30], as observed for even parity.

Complementary information is obtained from the distribution $P^k(r)$ of non-overlapping k -order gap ratios,

$$r_n^k = \frac{\min(\tilde{s}_n^k, \tilde{s}_{n+k}^k)}{\max(\tilde{s}_n^k, \tilde{s}_{n+k}^k)}, \quad (3)$$

which do not require unfolding [29, 30, 41, 42].

The spacing distributions are fitted to the function

$$P^k(s, \beta) \approx C_\alpha s^\alpha \exp[-A_\alpha s^2], \quad (4)$$

with α as the only free parameter since the coefficients A_α and C_α are fixed by the conditions $\int P^k(s) ds = 1$ and $\int s P^k(s) ds = \langle s \rangle = 1$. Within the simplest approximation of the Wigner surmise generalized to arbitrary order k , the exponent α is given by [29, 30]

$$\alpha(\beta, k) = \frac{k(k+1)}{2} \beta + k - 1, \quad (5)$$

where the Dyson index takes values $\beta = 1, 2, 4$ for the GOE, GUE, GSE respectively. The effective index β^* and order k^* , which best describe the numerical results,

are obtained by comparing the fitted value α_{fit} to an improved version of Eq. (5) [32, 43]. The analogue of Eqs. (4) and (5) for non-overlapping gap ratios is given in Refs. [29, 42, 44].

A complication arises when the spectrum is the superposition of m independent subsequences, as can occur due to unresolved symmetries or Hilbert-space fragmentation. Levels belonging to different subsequences do not repel, causing 1NN statistics to appear closer to the Poisson distribution even when each subsequence is well described by a Gaussian ensemble [45–48]. To determine m , in addition to the fitting procedure described above, we also compare against the distribution $P^k(s/r, \beta, m)$, the superposition of m independent blocks with index β . We write $P^k(s/r, \beta, 1) = P^k(s/r, \beta)$ for a single block. The distributions $P^k(s/r, \beta, m)$ are generated by Monte Carlo sampling and the closest matching one as a function of m is chosen by minimizing the Kolmogorov-Smirnov distance [49, 50] and the mean-square deviation [32].

An additional subtlety is that distinct ensembles at different orders can yield identical spectral statistics. A prominent example is the equivalence between the 2NN statistics of two superposed GOE blocks and those of a single GUE one: $P^{2k}(s/r, 1, 2) = P^k(s/r, 2)$ [29, 45]. Other similar inter-relationships between multi-block distributions [31, 45, 51–54] are encountered below.

Results—As shown in Fig. 1(b), for even total particle number $N = N_{\uparrow} + N_{\downarrow}$, the eigenvalues are non-degenerate. In contrast, in the odd- N sector the spectrum is composed of exact doublets ($E_{2l}, E_{2l+1} = E_{2l}$) [Fig. 1(c)]. This pairing occurs throughout the (λ_2, λ_3) plane [32] and survives after resolving all known mutually commuting conserved quantities ($N_{\uparrow}, N_{\downarrow}, k_x, k_y, f, S, B$). It is interesting to note that local observables such as spin and particle densities are related within each degenerate doublet by a flip $1 \leftrightarrow 2$ of the band (Wannier) index n [32]. Since S^z is fixed, these degeneracies are not due to the usual spin- $\frac{1}{2}$ time-reversal symmetry. In the limit $\lambda_2 = \lambda_3 = 0$, the spectrum is highly degenerate [Fig. 1(d)], due to the LIOMs of $\hat{\mathcal{H}}_{0,0}$ [17, 20].

A pronounced parity dependence appears in the spectral statistics. Figure 2 shows the k NN level spacing and gap ratio distributions for an even- N sector on an $N_x, N_y = 3, 2$ lattice. Both $P(s)$ and $P(r)$ are well described by $P^k(s/r, 1, 4)$, namely the superposition of four GOE blocks. For $k = 1$, the distribution is close to Poissonian, especially seen in the gap ratio, while the difference becomes clearer at higher orders. This behavior is consistent with the presence of LIOMs, which may explain the observed signatures of quasiparticle localization [20]. Fig. 2 illustrates also the relations $P^1(s/r, 1) = P^2(s/r, 1, 4)$ and $P^2(s/r, 1) = P^1(s/r, 4) = P^4(s/r, 1, 4)$ between different combinations (k, β, m) [45, 53, 54].

The odd- N sector, shown in Fig. 3 for the same lattice size $N_x, N_y = 3, 2$, displays qualitatively different behavior. The 1NN spacing distribution exhibits a pronounced peak at $s = 0$ due to the complete double degeneracy, thus higher ($k > 1$) order statistics are appro-

k	$N_x, N_y = 3, 2$	$N_x, N_y = 4, 2$	$N_x, N_y = 3, 3$	sing. part. hopping
Even	(1; 1, 4) 0.389	(1; 1, 6) 0.388	(1; 1, 2) 0.419	(1; 1) 0.528
	2 (1; 1) = (2; 1, 4) 0.529	(2; 1, 6) 0.508	(1; 2) = (2; 1, 2) 0.599	(2; 1) 0.675
	(3; 1, 4) 0.622	(1; 2) \sim (3; 1, 6) 0.580	(2; 1) = (3; 1, 2) 0.680	(3; 1) 0.746
	4 (2; 1) = (4; 1, 4) 0.676	(4; 1, 6) 0.633	(2; 2) = (4; 1, 2) 0.731	(4; 1) 0.789
Odd	1 DD	DD	DD	(1; 1) 0.530
	2 (1; 2) = (2; 1, 2) 0.596	(1; 2) = (2; 1, 2) 0.598	(1; 2) = (2; 1, 2) 0.592	(2; 1) 0.672
	3 — 0.507	— 0.508	— 0.508	(3; 1) 0.744
	4 (2; 2) = (4; 1, 2) 0.731	(2; 2) = (4; 1, 2) 0.735	(2; 2) = (4; 1, 2) 0.732	(4; 1) 0.791

TABLE I. Level statistics of the projected dice lattice Hamiltonian, grouped by the parity of $N = N_{\uparrow} + N_{\downarrow}$. Columns indicate the cluster size (N_x, N_y) (and the single-particle-hopping-augmented case for system size 3×2 , last column); rows correspond to different orders $k = 1, 2, 3, 4$. Each cell reports, on the top line, the best-matching RMT identification either as an effective single block (k^*, β^*) or as the superposition of m blocks $(k; \beta, m)$. The equality sign denotes relations between different multi-block distributions [53, 54]. The bottom line gives the k -order mean nonoverlapping gap ratio $\langle r^k \rangle$ computed in the largest accessible symmetry-resolved sector. DD denotes exact double degeneracy of all levels.

priate. Surprisingly, both 2NN and 4NN spacing and gap ratio distributions match the GUE at effective orders $k^* = 1$ and $k^* = 2$, respectively, which is equivalent to the superposition of two GOE blocks, since $P^{2k^*}(s/r, 1, 2) = P^{k^*}(s/r, 2)$ [29, 45]. By contrast, the 3NN spectral statistics does not resemble any m -block distribution, ruling out that the GUE behavior observed for $k = 2, 4$ can be explained by the superposition of two GOE blocks.

The phenomenology of the observed spectral statistics for different system sizes is summarized in Tab. I. In the even- N sector, all clusters studied display level statistics consistent with multi-block GOE behavior. Crucially, the inferred block number m varies with the size, consistent with the presence of an extensive number of LIOMs, possibly at the root of the nonergodic behavior observed previously [20]. However, the number of blocks does not increase monotonically with system size, being $m = 6$ for the 4×2 cluster and just $m = 2$ for 3×3 [32]. This may be a finite-size effect due to the small system sizes that are feasible with exact diagonalization. By contrast, both the complete double degeneracy and GUE behavior in the 2NN and 4NN statistics are present in the odd- N sector for all system sizes. Again, the 3NN distributions and the double degeneracy are incompatible with the superposition of two GOE blocks, and an alternative explanation is required for the GUE behavior.

Finally, the last column of Table I illustrates how the addition of a quadratic hopping term [32] leads to a rapid

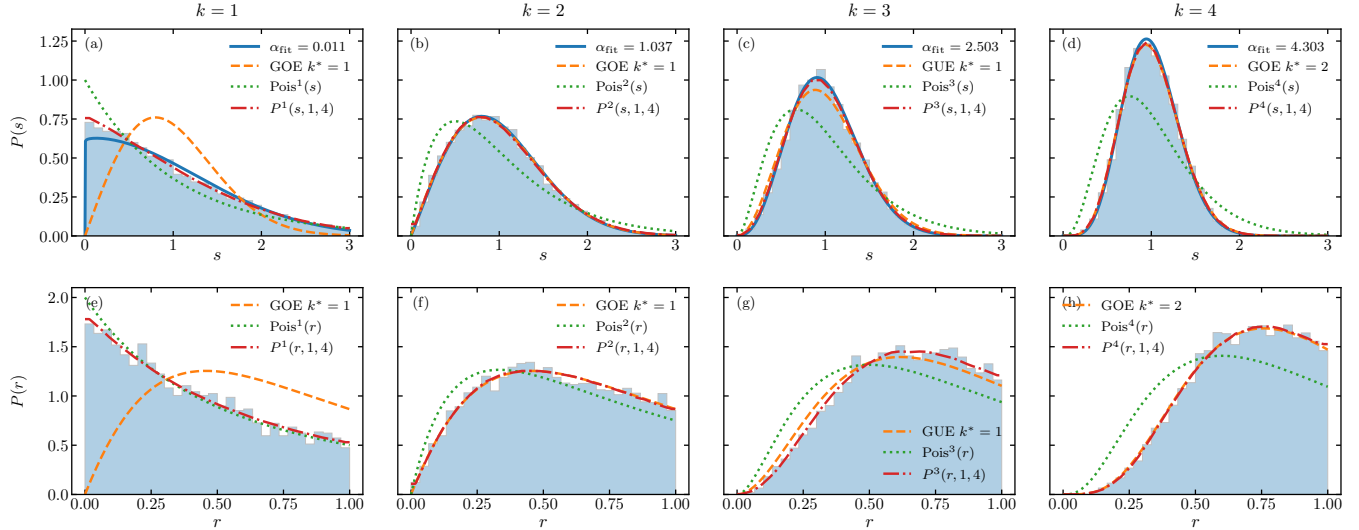


FIG. 2. Level spacing (top) and gap ratio (bottom) statistics of $\hat{\mathcal{H}}_{1,1}$ for even- N , size $N_x, N_y = 3, 2$, and quantum numbers $(N_\uparrow, N_\downarrow, k_x, k_y, f, S, B) = (6, 6, 0, 0, +, 0, 1)$ (Hilbert-space dimension $\mathcal{N} = 16529$). In the top row, the solid line shows the fit to (4). In both rows, the dashed curve is the closest matching Wigner surmise with effective order k^* (ensemble β^*). The dotted curve shows the k NN Poisson distribution, and the dash-dot curve is the closest m -block GOE distribution for each k . Both level-spacing and gap-ratio distributions are consistent with the superposition of four GOE spectra for any k . Note that $P(s/r, 1) = P^2(s/r, 1, 4)$ as seen in (b) and (f), while $P^2(s/r, 1) = P^4(s/r, 1, 4)$ from (d) and (h).

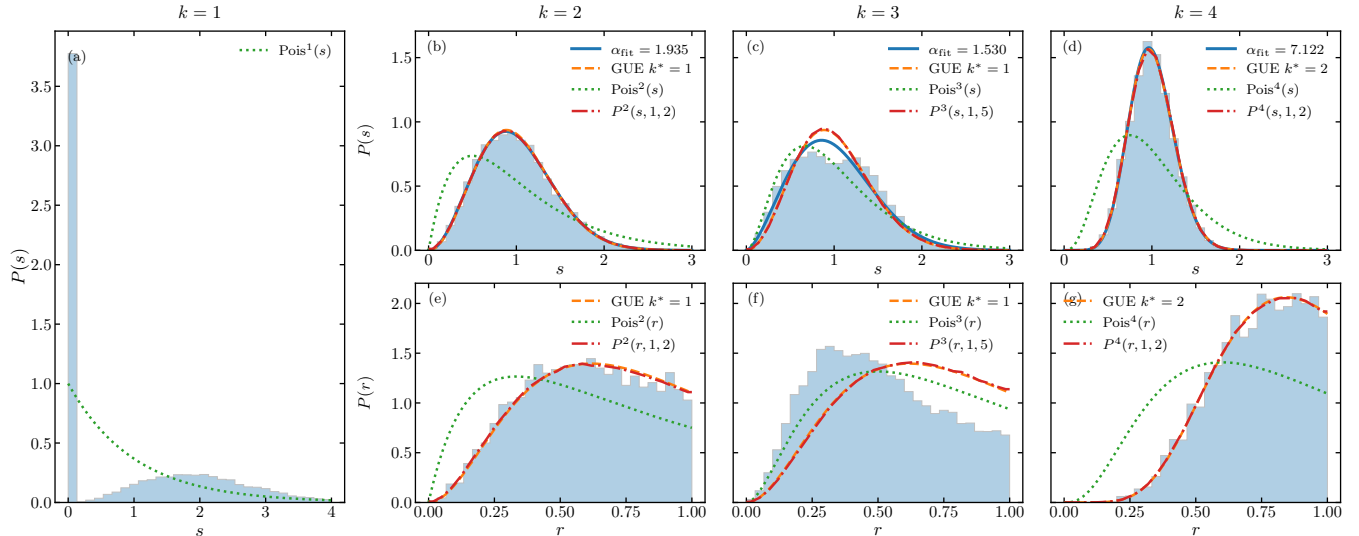


FIG. 3. Same as Fig. 2, but for odd- N and quantum numbers $(N_\uparrow, N_\downarrow, k_x, k_y, S, B) = (5, 6, 0, 0, 1/2, 1/2)$ (dimension $\mathcal{N} = 25176$). For $k = 1$, the double degeneracy leads to a pronounced peak at $s = 0$ in the level-spacing distribution and identically zero gap ratio (3) (not depicted). The $k = 2, 4$ statistics are very well described by the GUE with $k^* = 1, 2$, equivalent to the superposition of two GOE blocks due to the known relation $P^{2k^*}(s/r, 1, 2) = P^{k^*}(s/r, 2)$. However, the $k = 3$ case clearly deviates from the superposition of two GOE blocks. Note the relation $P(s/r, 2) = P^3(s/r, 1, 5)$ in (c) and (f).

loss of all parity- and size-dependent effects, rapidly driving the spectral statistics towards a single-block GOE distribution expected for a generic time-reversal and rotationally symmetric Hamiltonian without unresolved symmetries. Indeed, the complete double degeneracy of the spectrum, the GUE correlations in the 2NN and 4NN

distributions for odd parity, and the size-dependent block number m for even parity are exceptional and interesting features of the present model.

Discussion—A key open problem is to identify the mechanism enforcing the complete double degeneracy of the spectrum for odd parity. This is crucial since it most

likely underpins all other unusual phenomena observed in the spectral statistics. At present, we have uncovered at least two hints towards the solution. The first is that the states in a degenerate doublet are related by the exchange of the two nonequivalent Wannier functions shown in Fig. 1(a), in the same way as the states in a Kramers pair are related by a spin flip $S^z \rightarrow -S^z$ [55]. This would be consistent with a hidden antiunitary symmetry involving the band degree of freedom that would explain the degeneracy through Kramers' theorem.

The second piece of evidence is that the double degeneracy is present in the full dice lattice with a Hubbard interaction, even before the projection to the flat-band subspace. This is useful as it may be easier to pinpoint the antiunitary symmetry in the full model rather than in the projected one. This observation also suggests that it would be interesting to perform the spectral statistics analysis on the full model to see if the GUE spectral correlations and the block structure persist. Due to the large unit cell of the dice lattice with π -flux, it is not feasible to perform a full diagonalization of the Hamiltonian; one has to employ methods that can compute at least a few thousand eigenvalues in a large Hilbert space [56–58].

Alternatively, an intriguing possibility is that the degeneracy may be of topological origin. A relevant example is the Hamiltonian associated with the toric code [59],

since all of its eigenvalues (not just the ground state) are 4^g -fold degenerate on a surface of genus g . This would imply that this minimal interacting flat-band model features a parity-dependent topological order.

Another important open question is whether the observed spectral features are exclusive to the dice lattice or can be found in other lattice models with flat bands. Of particular interest are models realized experimentally, such as the kagome and Lieb lattices [60–64] or bands of moiré materials. Note that realistic proposals for realizing the dice lattice with π -flux using ultracold gases in optical lattices have been put forward [65–67], prompting further investigations on how the spectral features uncovered in this work may be observed in ultracold quantum simulators. A promising observable to consider is the particle counting statistics, which in a recent experiment with trapped Fermi gases are found in remarkable agreement with RMT predictions [68].

Acknowledgments—We acknowledge support from the Research Council of Finland under Grants No. 330384, No. 336369, and No. 358150, the Finnish Ministry of Education and Culture through the Quantum Doctoral Education Pilot Program (QDOC VN/3137/2024-OKM-4), and the Finnish Quantum Flagship (project No. 358877). We acknowledge the computational resources provided by the Aalto Science-IT project.

[1] Y. Cao, V. Fatemi, S. Fang, K. Watanabe, T. Taniguchi, E. Kaxiras, and P. Jarillo-Herrero, Unconventional superconductivity in magic-angle graphene superlattices, *Nature* **556**, 43 (2018).

[2] L. Balents, C. R. Dean, D. K. Efetov, and A. F. Young, Superconductivity and strong correlations in moiré flat bands, *Nature Physics* **16**, 725 (2020).

[3] E. Y. Andrei, D. K. Efetov, P. Jarillo-Herrero, A. H. MacDonald, K. F. Mak, T. Senthil, E. Tutuc, A. Yazdani, and A. F. Young, The marvels of moiré materials, *Nature Reviews Materials* **6**, 201 (2021).

[4] Y. Cao, J. M. Park, K. Watanabe, T. Taniguchi, and P. Jarillo-Herrero, Pauli-limit violation and re-entrant superconductivity in moiré graphene, *Nature* **595**, 526–531 (2021).

[5] J. M. Park, S. Sun, K. Watanabe, T. Taniguchi, and P. Jarillo-Herrero, Experimental evidence for nodal superconducting gap in moiré graphene, *Science* **391**, 79–83 (2026).

[6] H. Zhou, T. Xie, T. Taniguchi, K. Watanabe, and A. F. Young, Superconductivity in rhombohedral trilayer graphene, *Nature* **598**, 434–438 (2021).

[7] T. Han, Z. Lu, Z. Hadjri, L. Shi, Z. Wu, W. Xu, Y. Yao, A. A. Cotten, O. Sharifi Sedeh, H. Weldeyesus, J. Yang, J. Seo, S. Ye, M. Zhou, H. Liu, G. Shi, Z. Hua, K. Watanabe, T. Taniguchi, P. Xiong, D. M. Zumbühl, L. Fu, and L. Ju, Signatures of chiral superconductivity in rhombohedral graphene, *Nature* **643**, 654–661 (2025).

[8] L. Wang, Y. Gao, B. Wen, Z. Han, T. Taniguchi, K. Watanabe, M. Koshino, J. Hone, and C. R. Dean, Evidence for a fractional fractal quantum Hall effect in graphene superlattices, *Science* **350**, 1231 (2015).

[9] Z. Lu, T. Han, Y. Yao, A. P. Reddy, J. Yang, J. Seo, K. Watanabe, T. Taniguchi, L. Fu, and L. Ju, Fractional quantum anomalous Hall effect in multilayer graphene, *Nature* **626**, 759 (2024).

[10] D. Kim, S. Jin, T. Taniguchi, K. Watanabe, J. H. Smet, G. Y. Cho, and Y. Kim, Observation of 1/3 fractional quantum Hall physics in balanced large angle twisted bilayer graphene, *Nature Communications* **16**, 179 (2025).

[11] J. Zhao, L. Liu, Y. Zhang, H. Zhang, Z. Feng, C. Wang, S. Lai, G. Chang, B. Yang, and W. Gao, Exploring the Fractional Quantum Anomalous Hall Effect in Moiré Materials: Advances and Future Perspectives, *ACS Nano* **19**, 19509 (2025).

[12] S. D. Huber and E. Altman, Bose condensation in flat bands, *Physical Review B* **82**, 184502 (2010).

[13] G. Möller and N. R. Cooper, Correlated Phases of Bosons in the Flat Lowest Band of the Dice Lattice, *Physical Review Letters* **108**, 045306 (2012).

[14] O. Derzhko, J. Richter, and M. Maksymenko, Strongly correlated flat-band systems: The route from Heisenberg spins to Hubbard electrons, *International Journal of Modern Physics B* **29**, 1530007 (2015).

[15] M. Tovmasyan, S. Peotta, P. Törmä, and S. D. Huber, Effective theory and emergent $SU(2)$ symmetry in the flat bands of attractive Hubbard models, *Physical Review B* **94**, 245149 (2016).

[16] D. Leykam, A. Andrianov, and S. Flach, Artificial flat band systems: From lattice models to experiments, *Advances in Physics: X* **3**, 1473052 (2018).

[17] M. Tovmasyan, S. Peotta, L. Liang, P. Törmä, and S. D.

Huber, Preformed pairs in flat Bloch bands, *Physical Review B* **98**, 134513 (2018).

[18] Y. Kuno, T. Orito, and I. Ichinose, Flat-band many-body localization and ergodicity breaking in the Creutz ladder, *New Journal of Physics* **22**, 013032 (2020).

[19] E. Nicolau, A. M. Marques, R. G. Dias, and V. Ahufinger, Flat band induced local Hilbert space fragmentation, *Physical Review B* **108**, 205104 (2023).

[20] K. Swaminathan, P. Tadros, and S. Peotta, Signatures of many-body localization of quasiparticles in a flat band superconductor, *Physical Review Research* **5**, 043215 (2023).

[21] J. Vidal, R. Mosseri, and B. Douçot, Aharonov-Bohm Cages in Two-Dimensional Structures, *Physical Review Letters* **81**, 5888 (1998).

[22] J. Vidal, P. Butaud, B. Douçot, and R. Mosseri, Disorder and interactions in Aharonov-Bohm cages, *Physical Review B* **64**, 155306 (2001).

[23] T. Guhr, A. Müller-Groeling, and H. A. Weidenmüller, Random-matrix theories in quantum physics: Common concepts, *Physics Reports* **299**, 189 (1998).

[24] F. Haake, *Quantum Signatures of Chaos*, Springer Series in Synergetics, Vol. 54 (Springer Berlin Heidelberg, Berlin, Heidelberg, 2010).

[25] M. L. Mehta, *Random Matrices*, 3rd ed., Pure and Applied Mathematics, Vol. 142 (Academic Press, 2004).

[26] P. Sala, T. Rakovszky, R. Verresen, M. Knap, and F. Pollmann, Ergodicity Breaking Arising from Hilbert Space Fragmentation in Dipole-Conserving Hamiltonians, *Physical Review X* **10**, 011047 (2020).

[27] S. Moudgalya and O. I. Motrunich, Hilbert Space Fragmentation and Commutant Algebras, *Physical Review X* **12**, 011050 (2022).

[28] S. Moudgalya, B. A. Bernevig, and N. Regnault, Quantum many-body scars and Hilbert space fragmentation: A review of exact results, *Reports on Progress in Physics* **85**, 086501 (2022).

[29] S. H. Tekur, U. T. Bhosale, and M. S. Santhanam, Higher-order spacing ratios in random matrix theory and complex quantum systems, *Physical Review B* **98**, 104305 (2018).

[30] W.-J. Rao, Higher-order level spacings in random matrix theory based on Wigner's conjecture, *Physical Review B* **102**, 054202 (2020).

[31] F. He, A. Hutsalyuk, G. Mussardo, and A. Stampiggi, *Statistical Signatures of Integrable and Non-Integrable Quantum Hamiltonians* (2025), arXiv:2510.02440 [cond-mat].

[32] See Supplemental Material [URL] for the explicit representation of the Hamiltonian, details on the unfolding procedure and spectral statistics analysis, and additional supporting results. Refs. [69–74] are included in this Supplementary Material.

[33] S. M. Zhang and L. Jin, Compact localized states and localization dynamics in the dice lattice, *Physical Review B* **102**, 054301 (2020).

[34] A. O. Barut and A. Böhm, Dynamical Groups and Mass Formula, *Physical Review* **139**, B1107 (1965).

[35] B. Buča, J. Tindall, and D. Jaksch, Non-stationary coherent quantum many-body dynamics through dissipation, *Nature Communications* **10**, 1730 (2019).

[36] P. Weinberg and M. Bukov, QuSpin: A Python package for dynamics and exact diagonalisation of quantum many body systems part I: Spin chains, *SciPost Physics* **2**, 003 (2017).

[37] P. Weinberg and M. Bukov, QuSpin: A Python package for dynamics and exact diagonalisation of quantum many body systems. Part II: Bosons, fermions and higher spins, *SciPost Physics* **7**, 020 (2019).

[38] D. Poilblanc, T. Ziman, J. Bellissard, F. Mila, and G. Montambaux, Poisson vs. GOE Statistics in Integrable and Non-Integrable Quantum Hamiltonians, *Europhysics Letters* **22**, 537 (1993).

[39] M. Teeriah, V.-V. Linho, K. Swaminathan, and S. Peotta, Coexistence of ergodic and nonergodic behavior and level spacing statistics in a one-dimensional model of a flat band superconductor, *Physical Review Research* **7**, 013318 (2025).

[40] L. F. Santos, Integrability of a disordered Heisenberg spin-1/2 chain, *Journal of Physics A: Mathematical and General* **37**, 4723 (2004).

[41] V. Oganesyan and D. A. Huse, Localization of interacting fermions at high temperature, *Physical Review B* **75**, 155111 (2007).

[42] Y. Y. Atas, E. Bogomolny, O. Giraud, and G. Roux, Distribution of the Ratio of Consecutive Level Spacings in Random Matrix Ensembles, *Physical Review Letters* **110**, 084101 (2013).

[43] R. Shir, P. Martinez-Azcona, and A. Chenu, Surmise for random matrices' level spacing distributions beyond nearest-neighbors, *Journal of Physics A: Mathematical and Theoretical* **58**, 445206 (2025).

[44] Y. Y. Atas, E. Bogomolny, O. Giraud, P. Vivo, and E. Vivo, Joint probability densities of level spacing ratios in random matrices, *Journal of Physics A: Mathematical and Theoretical* **46**, 355204 (2013).

[45] P. Bleher and A. R. Its, *Random Matrix Models and Their Applications*, Mathematical Sciences Research Institute Publications No. 40 (Cambridge university press, Cambridge, 2001).

[46] G. W. Anderson, A. Guionnet, and O. Zeitouni, *An Introduction to Random Matrices*, 1st ed. (Cambridge University Press, 2009).

[47] P. Deift and P. J. Forrester, eds., *Random Matrix Theory, Interacting Particle Systems, and Integrable Systems*, Mathematical Sciences Research Institute Publications No. 65 (Cambridge University Press, Cambridge, 2014).

[48] O. Giraud, N. Macé, É. Vernier, and F. Alet, Probing Symmetries of Quantum Many-Body Systems through Gap Ratio Statistics, *Physical Review X* **12**, 011006 (2022).

[49] F. J. Massey, The Kolmogorov-Smirnov Test for Goodness of Fit, *Journal of the American Statistical Association* **46**, 68 (1951).

[50] M. A. Stephens, EDF Statistics for Goodness of Fit and Some Comparisons, *Journal of the American Statistical Association* **69**, 730 (1974).

[51] P. J. Forrester and E. M. Rains, Correlations for superpositions and decimations of Laguerre and Jacobi orthogonal matrix ensembles with a parameter, *Probability Theory and Related Fields* **130**, 518 (2004).

[52] P. J. Forrester, A Random Matrix Decimation Procedure Relating $\beta = 2/(r+1)$ to $\beta = 2(r+1)$, *Communications in Mathematical Physics* **285**, 653 (2009).

[53] S. H. Tekur and M. S. Santhanam, Symmetry deduction from spectral fluctuations in complex quantum systems,

Physical Review Research **2**, 032063 (2020).

[54] U. T. Bhosale, Superposition and higher-order spacing ratios in random matrix theory with application to complex systems, *Physical Review B* **104**, 054204 (2021).

[55] J. J. Sakurai and J. Napolitano, *Modern Quantum Mechanics*, 3rd ed. (Cambridge University Press, 2020).

[56] F. Pietracaprina, N. Macé, D. J. Luitz, and F. Alet, Shift-invert diagonalization of large many-body localizing spin chains, *SciPost Physics* **5**, 045 (2018).

[57] P. Sierant, M. Lewenstein, and J. Zakrzewski, Polynomially Filtered Exact Diagonalization Approach to Many-Body Localization, *Physical Review Letters* **125**, 156601 (2020).

[58] H. Guan and W. Zhang, Dual applications of Chebyshev polynomials method: Efficiently finding thousands of central eigenvalues for many-spin systems, *SciPost Physics* **11**, 103 (2021).

[59] A. Yu. Kitaev, Fault-tolerant quantum computation by anyons, *Annals of Physics* **303**, 2 (2003).

[60] G.-B. Jo, J. Guzman, C. K. Thomas, P. Hosur, A. Vishwanath, and D. M. Stamper-Kurn, Ultracold Atoms in a Tunable Optical Kagome Lattice, *Physical Review Letters* **108**, 045305 (2012).

[61] C. K. Thomas, T. H. Barter, T.-H. Leung, M. Okano, G.-B. Jo, J. Guzman, I. Kimchi, A. Vishwanath, and D. M. Stamper-Kurn, Mean-Field Scaling of the Superfluid to Mott Insulator Transition in a 2D Optical Superlattice, *Physical Review Letters* **119**, 100402 (2017).

[62] T.-H. Leung, M. N. Schwarz, S.-W. Chang, C. D. Brown, G. Unnikrishnan, and D. Stamper-Kurn, Interaction-Enhanced Group Velocity of Bosons in the Flat Band of an Optical Kagome Lattice, *Physical Review Letters* **125**, 133001 (2020).

[63] S. Taie, H. Ozawa, T. Ichinose, T. Nishio, S. Nakajima, and Y. Takahashi, Coherent driving and freezing of bosonic matter wave in an optical Lieb lattice, *Science Advances* **1**, e1500854 (2015).

[64] S. Taie, T. Ichinose, H. Ozawa, and Y. Takahashi, Spatial adiabatic passage of massive quantum particles in an optical Lieb lattice, *Nature Communications* **11**, 257 (2020).

[65] T. Andrijauskas, E. Anisimovas, M. Račiūnas, A. Mekys, V. Kudriašov, I. B. Spielman, and G. Juzeliūnas, Three-level Haldane-like model on a dice optical lattice, *Physical Review A* **92**, 033617 (2015).

[66] G. Möller and N. R. Cooper, Synthetic gauge fields for lattices with multi-orbital unit cells: Routes towards a π -flux dice lattice with flat bands, *New Journal of Physics* **20**, 073025 (2018).

[67] C. Tassi and D. Bercioux, Implementation and Characterization of the Dice Lattice in the Electron Quantum Simulator, *Advanced Physics Research* **3**, 2400038 (2024).

[68] M. Dixmerias, G. D. V. D. Vecchio, C. Daix, J. Verstraten, T. de Jongh, B. Peaudecerf, P. L. Doussal, G. Schehr, and T. Yefsah, Universal Random Matrix Behavior of a Fermionic Quantum Gas (2025), arXiv:2510.25735 [cond-mat].

[69] T. A. Brody, J. Flores, J. B. French, P. A. Mello, A. Pandey, and S. S. M. Wong, Random-matrix physics: Spectrum and strength fluctuations, *Reviews of Modern Physics* **53**, 385 (1981).

[70] F. J. Dyson and M. L. Mehta, Statistical Theory of the Energy Levels of Complex Systems. IV, *Journal of Mathematical Physics* **4**, 701 (1963).

[71] I. Dumitriu and A. Edelman, Matrix models for beta ensembles, *Journal of Mathematical Physics* **43**, 5830 (2002).

[72] B. Chakrabarti, A. Biswas, V. K. B. Kota, K. Roy, and S. K. Haldar, Energy-level statistics of interacting trapped bosons, *Physical Review A* **86**, 013637 (2012).

[73] A. Kapustin and L. Fidkowski, Local Commuting Projector Hamiltonians and the Quantum Hall Effect, *Communications in Mathematical Physics* **373**, 763 (2020).

[74] A. D. Kerin, B. Dietz, and J. Brand, Quartic level repulsion in a quantum chaotic three-body system without symplectic symmetry (2025), arXiv:2510.06772 [cond-mat].

Supplemental Material for “Parity-dependent double degeneracy and spectral statistics in the projected dice lattice”

This Supplemental section presents the explicit representation and symmetry properties of the projected dice lattice Hamiltonian studied in the main text, along with details on the unfolding procedure, spectral statistics analysis, and additional supporting results, in particular, the spectral statistics analysis for the different system sizes used to fill the entries of Tab. I in the main text. We follow the notation of Ref. [1].

I. PROJECTED DICE LATTICE HAMILTONIAN

We consider the dice lattice threaded by a π -flux per rhombus, for which all bands are flat and two by two degenerate. The dice lattice single-particle Hamiltonian is represented graphically in the left panel of Fig. 1. Projecting an attractive on-site Hubbard interaction onto the subspace corresponding to the two lowest flat bands yields an effective many-body Hamiltonian acting on a much smaller Hilbert space, thus enabling exact diagonalization of finite clusters with sufficiently large size. For practical computations, it is convenient to work with an orthonormal Wannier basis of the projected subspace and the corresponding canonical fermionic operators. The flat bands admit compactly localized Wannier functions $w_{n\mathbf{l}}$, where $n = 1, 2$ labels the two Wannier orbitals per unit cell and the pair of integers $\mathbf{l} = (l_x, l_y)$ labels the unit cell. We denote by $\hat{d}_{n\mathbf{l}\sigma}$ the fermionic annihilation operator for a fermion with spin $\sigma = \uparrow, \downarrow$ in Wannier state $w_{n\mathbf{l}}$. Compact localization of $w_{n\mathbf{l}}$ is a key simplifying feature of the dice lattice and underlies the short-range structure of the projected Hamiltonian [1–3].

For each Wannier state, we define the spin-resolved and total density operators

$$\hat{\rho}_{n\mathbf{l}\sigma} = \hat{d}_{n\mathbf{l}\sigma}^\dagger \hat{d}_{n\mathbf{l}\sigma}, \quad \hat{\rho}_{n\mathbf{l}} = \hat{\rho}_{n\mathbf{l}\uparrow} + \hat{\rho}_{n\mathbf{l}\downarrow}, \quad (1)$$

on-site spin operators

$$\hat{S}_{n\mathbf{l}}^+ = \hat{d}_{n\mathbf{l}\uparrow}^\dagger \hat{d}_{n\mathbf{l}\downarrow}, \quad \hat{S}_{n\mathbf{l}}^- = (\hat{S}_{n\mathbf{l}}^+)^{\dagger}, \quad \hat{S}_{n\mathbf{l}}^x = \frac{1}{2}(\hat{S}_{n\mathbf{l}}^+ + \hat{S}_{n\mathbf{l}}^-), \quad \hat{S}_{n\mathbf{l}}^y = \frac{1}{2i}(\hat{S}_{n\mathbf{l}}^+ - \hat{S}_{n\mathbf{l}}^-), \quad \hat{S}_{n\mathbf{l}}^z = \frac{1}{2}(\hat{\rho}_{n\mathbf{l}\uparrow} - \hat{\rho}_{n\mathbf{l}\downarrow}), \quad (2)$$

and on-site pair (pseudospin) operators

$$\hat{B}_{n\mathbf{l}}^+ = \hat{d}_{n\mathbf{l}\uparrow}^\dagger \hat{d}_{n\mathbf{l}\downarrow}^\dagger, \quad \hat{B}_{n\mathbf{l}}^- = (\hat{B}_{n\mathbf{l}}^+)^{\dagger}, \quad \hat{B}_{n\mathbf{l}}^x = \frac{1}{2}(\hat{B}_{n\mathbf{l}}^+ + \hat{B}_{n\mathbf{l}}^-), \quad \hat{B}_{n\mathbf{l}}^y = \frac{1}{2i}(\hat{B}_{n\mathbf{l}}^+ - \hat{B}_{n\mathbf{l}}^-), \quad \hat{B}_{n\mathbf{l}}^z = \frac{1}{2}(\hat{\rho}_{n\mathbf{l}} - 1). \quad (3)$$

Each of the sets of operators $\hat{\mathbf{S}}_{n\mathbf{l}} = (\hat{S}_{n\mathbf{l}}^x, \hat{S}_{n\mathbf{l}}^y, \hat{S}_{n\mathbf{l}}^z)^T$ and $\hat{\mathbf{B}}_{n\mathbf{l}} = (\hat{B}_{n\mathbf{l}}^x, \hat{B}_{n\mathbf{l}}^y, \hat{B}_{n\mathbf{l}}^z)^T$ generates an SU(2) algebra and they commute with each other $[\hat{S}_{n\mathbf{l}}^\alpha, \hat{B}_{n'\mathbf{l}'}^\beta] = 0$.

Pairs of particles living on nearest-neighbor Wannier functions, called bond singlets, are created by the operator

$$\hat{B}_{\langle n_1 \mathbf{l}_1, n_2 \mathbf{l}_2 \rangle}^+ = \hat{d}_{n_1 \mathbf{l}_1 \uparrow}^\dagger \hat{d}_{n_2 \mathbf{l}_2 \downarrow}^\dagger - \hat{d}_{n_1 \mathbf{l}_1 \downarrow}^\dagger \hat{d}_{n_2 \mathbf{l}_2 \uparrow}^\dagger, \quad (4)$$

with $\hat{B}_{\langle n_1 \mathbf{l}_1, n_2 \mathbf{l}_2 \rangle}^-$ its Hermitian conjugate. Here $\langle n_1 \mathbf{l}_1, n_2 \mathbf{l}_2 \rangle$ denotes a pair of overlapping nearest-neighbor Wannier functions, namely Wannier functions whose supports overlap on exactly two sites of the dice lattice.

The Hamiltonian obtained by projecting on the subspace of the two lowest flat bands can be presented as the sum of three contributions

$$\hat{\mathcal{H}}_{\lambda_2, \lambda_3} = \hat{\mathcal{H}}_{\text{tri.}} + \lambda_2 \hat{\mathcal{H}}_{\text{kag.}} + \lambda_3 \hat{\mathcal{H}}_{\text{tri.-kag.}}. \quad (5)$$

For convenience, the second and third terms are multiplied by the parameters λ_2 and λ_3 . The Hamiltonian obtained by the projection on the flat-band subspace is given by the choice $\lambda_2 = \lambda_3 = 1$.

The “triangular” term acts on spins and pseudospins on the triangular lattice of Wannier centers:

$$\begin{aligned} \hat{\mathcal{H}}_{\text{tri.}} &= -A \sum_{n, \mathbf{l}} \hat{B}_{n\mathbf{l}}^+ \hat{B}_{n\mathbf{l}}^- - 4 \sum_{\langle n\mathbf{l}, n'\mathbf{l}' \rangle} \left[\left(\hat{B}_{n\mathbf{l}}^z + \frac{1}{2} \right) \left(\hat{B}_{n'\mathbf{l}'}^z + \frac{1}{2} \right) + \frac{1}{2} \left(\hat{B}_{n\mathbf{l}}^+ \hat{B}_{n'\mathbf{l}'}^- + \hat{B}_{n\mathbf{l}}^- \hat{B}_{n'\mathbf{l}'}^+ \right) \right] \\ &+ 4 \sum_{\langle n\mathbf{l}, n'\mathbf{l}' \rangle} \left[\hat{S}_{n\mathbf{l}}^z \hat{S}_{n'\mathbf{l}'}^z + \frac{1}{2} \left(\hat{S}_{n\mathbf{l}}^+ \hat{S}_{n'\mathbf{l}'}^- + \hat{S}_{n\mathbf{l}}^- \hat{S}_{n'\mathbf{l}'}^+ \right) \right], \end{aligned} \quad (6)$$

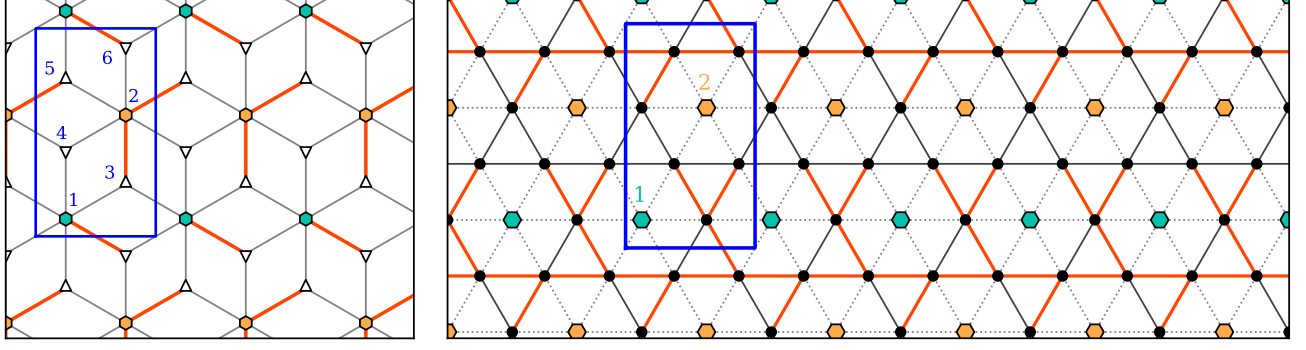


FIG. 1. (left) Schematic of the dice lattice. The magnetic unit cell is highlighted in the rectangular box with orbital indices $\alpha = 1, 2, 3, 4, 5, 6$. (right) Graphical representation of the term $\hat{\mathcal{H}}_{\text{tri.}} + \hat{\mathcal{H}}_{\text{kag.}}$ in the projected Hamiltonian $\hat{\mathcal{H}}_{\lambda_2, \lambda_3}$ (5). The Wannier functions $w_{n=1,1}$ and $w_{n=2,1}$ are represented by the turquoise and orange hexagons, respectively. One unit cell (shown as the blue rectangle) contains one turquoise site and one orange site, corresponding to the two nonequivalent Wannier functions. The dotted lines connecting turquoise and orange sites represent the nearest-neighbor interaction and hopping terms of on-site pairs and on-site spins in $\hat{\mathcal{H}}_{\text{tri.}}$ (6). In particular, the on-site pairs hop between nearest-neighbors in the triangular lattice composed of turquoise and orange sites. The black sites sit in the middle of the bonds connecting the turquoise and orange sites and form a kagome lattice. The operator $\hat{B}_{\langle n_1 l_1, n_2 l_2 \rangle}^+$ creates a singlet on the bond $\langle n_1 l_1, n_2 l_2 \rangle$, thus the bond singlets live on the kagome lattice formed by the black dots. The black and red bonds represent terms of the form $\hat{B}_{\langle n_1 l_1, n_2 l_2 \rangle}^+ \hat{B}_{\langle n_1 l_1, n_3 l_3 \rangle}^-$ in the bond-singlet hopping Hamiltonian $\hat{\mathcal{H}}_{\text{kag.}}$ (7). The sign of the hopping amplitude of the bonds connecting the black sites is given by $-s(n_1 l_1 | n_2 l_2, n_3 l_3)$ and is equal to -1 for the black bonds and to +1 for the red bonds. The terms of the form $\hat{B}_{n_1 l_1}^+ \hat{B}_{\langle n_2 l_2, n_3 l_3 \rangle}^-$ in $\hat{\mathcal{H}}_{\text{tri.-kag.}}$ (8) are not represented in this figure for clarity. Refer to the appendix in Ref. [1] instead.

where $A > 0$ sets the on-site pair binding energy. The value of A depends on the ratio between the Hubbard couplings on the three- and six-fold coordinated sites of the dice lattice (see left panel of Fig. 1) and does not have a qualitative effect on the results of this work, therefore it is always set to $A = 10$.

The “kagome” term describes the hopping of bond singlets living on the kagome lattice dual to the triangular bond network:

$$\hat{\mathcal{H}}_{\text{kag.}} = - \sum_{\langle 1,2,3 \rangle} \left[s(1|2,3) \left(\hat{B}_{\langle 1,2 \rangle}^+ \hat{B}_{\langle 1,3 \rangle}^- + \text{H.c.} \right) + \text{cyclic perm. of } (1,2,3) \right], \quad (7)$$

where $\langle 1, 2, 3 \rangle$ runs over unordered triplets of nearest-neighbor Wannier orbitals forming a triangle and the sign $s(1|2,3) = \pm 1$ encodes the overlap-induced sign structure controlling bond-singlet motion (see right panel of Fig. 1).

Finally, the “triangular-kagome” term converts on-site pairs into bond singlets and vice versa:

$$\hat{\mathcal{H}}_{\text{tri.-kag.}} = - \sum_{\langle 1,2,3 \rangle} \left[s(1|2,3) \left(\hat{B}_{\langle 1,2 \rangle}^+ \hat{B}_{\langle 2,3 \rangle}^- + \text{H.c.} \right) + \text{cyclic perm. of } (1,2,3) \right]. \quad (8)$$

A. Symmetries and symmetry resolution used in exact diagonalization

The projected Hamiltonian $\hat{\mathcal{H}}_{\lambda_2, \lambda_3}$ inherits a set of spatial and internal symmetries whose resolution is necessary before analyzing the level spacing statistics (LSS).

a. *Translations* The lattice translation operators \hat{T}_μ ($\mu = 1, 2$) satisfy the following commutation relations

$$\hat{T}_\mu \hat{d}_{n l \sigma} \hat{T}_\mu^\dagger = \hat{d}_{n, l + \mathbf{e}_\mu, \sigma}, \quad [\hat{\mathcal{H}}_{\lambda_2, \lambda_3}, \hat{T}_\mu] = 0, \quad (9)$$

where $\mathbf{e}_x = (1, 0)^T$ and $\mathbf{e}_y = (0, 1)^T$. On a system comprising of $N_x \times N_y$ unit cells, their eigenvalues take the form $\exp(2\pi i k_\mu / N_\mu)$, where k_μ are integers satisfying $0 \leq k_\mu \leq N_\mu$. The vector $\mathbf{k} = (k_x, k_y)$ is called here the crystal momentum, or simply momentum.

b. *Reflections and twofold rotation* As a consequence of the background π -flux, reflections are implemented as gauge-dressed permutation operations $\hat{R}_\nu = \hat{P}_\nu \hat{G}_\nu$ where \hat{P}_ν permutes the sites/orbitals according to a mirror symmetry and \hat{G}_ν is a diagonal \mathbb{Z}_2 gauge transformation. We use the convention that the \hat{R}_ν reflection flips the

unit-cell ν -index. It is convenient to define the gauge-dressed reflections in the single-particle Hilbert space of the full dice lattice spanned by the single-particle basis $|i_x, i_y, \alpha\rangle$ (unit-cell coordinates $(i_x, i_y) \in \mathbb{Z}^2$ and sublattice index $\alpha \in \{1, \dots, 6\}$, see left panel of Fig. 1). Let the symbols R_ν , P_ν and G_ν (without the “hat”) denote the single-particle operators corresponding to the Fock-space operators \hat{R}_ν , \hat{P}_ν and \hat{G}_ν . Then, the permutation operator P_ν is defined as

$$P_x |i_x, i_y, \alpha\rangle = \begin{cases} | -i_x, i_y, \alpha \rangle, & \alpha \in \{1, 4, 5\}, \\ | -i_x - 1, i_y, \alpha \rangle, & \alpha \in \{2, 3, 6\}, \end{cases} \quad (10)$$

for the mirror symmetry flipping i_x , while for i_y one has

$$P_y |i_x, i_y, \alpha\rangle = \begin{cases} | i_x, -i_y, 1 \rangle, & \alpha = 1, \\ | i_x, -i_y - 1, 2 \rangle, & \alpha = 2, \\ | i_x, -i_y - 1, 9 - \alpha \rangle, & \alpha \in \{3, 4, 5, 6\}, \end{cases} \quad (11)$$

The gauge transformations restore the π -flux hopping-sign pattern after the mirror symmetry has been applied and are defined by

$$G_x |i_x, i_y, \alpha\rangle = g_x(i_y, \alpha) |i_x, i_y, \alpha\rangle, \quad g_x(i_y, \alpha) = \begin{cases} (-1)^{i_y}, & \alpha \in \{1, 2, 3, 4, 6\}, \\ (-1)^{i_y+1}, & \alpha = 5, \end{cases} \quad (12)$$

and

$$G_y |i_x, i_y, \alpha\rangle = g_y(i_x, \alpha) |i_x, i_y, \alpha\rangle, \quad g_y(i_x, \alpha) = \begin{cases} (-1)^{i_x}, & \alpha \in \{1, 2, 4, 5\}, \\ (-1)^{i_x+1}, & \alpha \in \{3, 6\}. \end{cases} \quad (13)$$

Note that $G_{x(y)}$ can be defined only if $N_{y(x)}$ is even. The commutation relations between the mirror symmetry operators and the translation operators are the following

$$\hat{R}_\nu \hat{T}_\nu \hat{R}_\nu^{-1} = \hat{T}_\nu^{-1}, \quad \hat{R}_\nu \hat{T}_{\mu \neq \nu} \hat{R}_\nu^{-1} = -\hat{T}_\mu, \quad \mu, \nu = x, y. \quad (14)$$

The minus sign on the right-hand side of the second relation is a consequence of the gauge transformation \hat{G}_ν . The product of the two reflections $\hat{C}_2 = \hat{R}_x \hat{R}_y$ acts as a twofold rotation satisfying

$$\hat{C}_2 \hat{T}_\mu \hat{C}_2^{-1} = -\hat{T}_\mu^{-1}, \quad (15)$$

so that in momentum space \hat{C}_2 maps $\mathbf{k} \rightarrow -\mathbf{k} + (N_x/2, N_y/2)$ up to a reciprocal-lattice shift. As a result, \hat{C}_2 does not yield an independent quantum number in a generic momentum block, except at momenta invariant under this mapping.

c. Spin SU(2) symmetry. The model is invariant under global SU(2) spin rotations. Defining $\hat{S}^\alpha = \sum_{n,1} \hat{S}_{n1}^\alpha$ and $\hat{S}^2 = \sum_{\alpha=x,y,z} (\hat{S}^\alpha)^2$, one has

$$[\hat{\mathcal{H}}_{\lambda_2, \lambda_3}, \hat{S}^\alpha] = 0, \quad [\hat{\mathcal{H}}_{\lambda_2, \lambda_3}, \hat{S}^2] = 0. \quad (16)$$

In the numerics, we fix $S^z = N_\uparrow - N_\downarrow$ by working in a sector with a fixed number of particles N_\uparrow and N_\downarrow . When $N_\uparrow = N_\downarrow$, there is an additional spin-flip symmetry $S^z \rightarrow -S^z$ that further splits the space into two sectors labelled by $f \in \{+, -\}$.

d. Spectrum-generating algebra and pseudospin. An important feature of $\hat{\mathcal{H}}_{\lambda_2, \lambda_3}$ for $\lambda_2 = \lambda_3 = \lambda$ is the existence of the pair creation operator

$$\hat{B}^+ = \sum_{n,1} \hat{B}_{n1}^+ = \sum_{n,1} \hat{d}_{n1\uparrow}^\dagger \hat{d}_{n1\downarrow}^\dagger, \quad (17)$$

which acts as a ladder operator

$$[\hat{\mathcal{H}}_{\lambda, \lambda}, \hat{B}^+] = -E_p \hat{B}^+, \quad (18)$$

where E_p is the pair binding energy. This property allows the construction of broad families of exact eigenstates generated by repeated application of \hat{B}^+ . A consequence of (18) is that the total pseudospin operator $\hat{B}^2 = \sum_{\alpha=x,y,z} (\hat{B}^\alpha)^2$, with $\hat{B}^\alpha = \sum_{n,1} \hat{B}_{n1}^\alpha$, is also a conserved quantity.

e. *Local integrals of motion of $\hat{\mathcal{H}}_{0,0}$.* The triangular Hamiltonian alone ($\hat{\mathcal{H}}_{\text{tri.}} = \hat{\mathcal{H}}_{0,0}$) possesses an extensive set of strictly local conserved quantities. These are the total spin operators $\hat{S}_{nl}^2 = \sum_{\alpha=x,y,z} (\hat{S}_{nl}^{\alpha})^2$ of each Wannier function. This means that the occupancy pattern of singly occupied Wannier orbitals is conserved since the eigenvalue of \hat{S}_{nl}^2 is $3/4$ if exactly one particle is present in the Wannier function labeled by nl and zero if it is empty or doubly occupied. These local integrals of motions (LIOMs) do not commute with $\hat{\mathcal{H}}_{\lambda_2, \lambda_3}$ if λ_2 or λ_3 is nonzero, that is, when bond-singlet hopping and conversion are present, but they motivate the search for deformed LIOMs organizing the spectrum away from $\lambda_2 = \lambda_3 = 0$. Note that, due to the identity $\hat{S}_{nl}^2 + \hat{B}_{nl}^2 = \frac{3}{4}\hat{1}$, the operators \hat{B}_{nl}^2 do not form a set of independent conserved quantities.

f. *Time-reversal symmetry.* Since all Peierls phase factors in the single-particle dice lattice Hamiltonian are real, even after the projection, the model is invariant under the standard antiunitary time-reversal operator $\hat{\mathcal{T}}$ for spin- $\frac{1}{2}$,

$$\hat{\mathcal{T}}\hat{d}_{nl\uparrow}\hat{\mathcal{T}}^{-1} = \hat{d}_{nl\downarrow}, \quad \hat{\mathcal{T}}\hat{d}_{nl\downarrow}\hat{\mathcal{T}}^{-1} = -\hat{d}_{nl\uparrow}, \quad \hat{\mathcal{T}}^2 = -1, \quad \hat{\mathcal{T}}z = z^*\hat{\mathcal{T}}, \quad z \in \mathbb{C}. \quad (19)$$

Since $\hat{\mathcal{T}}$ flips S^z , the Kramers degeneracy does not appear within a fixed $(N_{\uparrow}, N_{\downarrow})$ sector. Time-reversal symmetry together with full spin rotational symmetry fixes the Dyson class, namely the Gaussian Orthogonal Ensemble (GOE), once all unitary symmetries are resolved [4].

g. *Symmetry resolution in exact diagonalization.* We diagonalize $\hat{\mathcal{H}}_{\lambda_2, \lambda_3}$ on a finite cluster comprising of $N_x \times N_y$ unit cells in a sector with quantum numbers $(N_{\uparrow}, N_{\downarrow}, \mathbf{k}, [f])$. The spin-flip quantum number is resolved only for $N_{\uparrow} = N_{\downarrow}$. We do not impose fixed total spin S or pseudospin B at the basis level in the numerics; instead, we resolve them using a penalty-term approach [5, 6], diagonalizing $\hat{\mathcal{H}}_{\lambda_2, \lambda_3} + \alpha \hat{S}^2 + \beta \hat{B}^2$ with sufficiently large positive α, β and subsequently selecting the desired (S, B) subsector, usually the one with the largest dimension. All computations were performed using the package QuSpin [7, 8].

II. DETAILS ON THE SPECTRAL STATISTICS ANALYSIS

To quantify spectral correlations of the fully symmetry-resolved many-body spectrum of $\hat{\mathcal{H}}_{\lambda_2, \lambda_3}$, we analyze k -order level spacings and nonoverlapping gap ratios. These are useful in the presence of exact degeneracies and multi-block structure. Our analysis follows and extends Refs. [9–13].

A. Ordered spectra and k -order spacings

For a fully symmetry-resolved sector characterized by quantum numbers $(N_{\uparrow}, N_{\downarrow}, \mathbf{k}, [f], S, B)$, the ordered eigenvalues $E_1 \leq E_2 \leq \dots \leq E_N$ are obtained from exact diagonalization. To reduce the impact of fluctuations associated with the edges of the spectrum, we discard a small fraction of levels at each end and retain only the bulk spectrum on which we perform the level-spacing and gap-ratio analysis. In practice, we discard the lowest and highest fraction $f_{\text{edge}} = 0.025$ of eigenvalues.

We define the raw k NN spacings by $\tilde{s}_n^k = E_{n+k} - E_n$, for $k = 1, 2, 3, 4$, and computed for all n such that both E_n and E_{n+k} lie in the retained bulk window. Because the density of states varies smoothly with energy, we remove this variation by unfolding, following the procedure of Refs. [6, 14]. We partition the retained spectrum into $q = 30$ disjoint, contiguous sets¹ with an equal number of levels. Within each set, we compute the local mean spacing $\langle \tilde{s}^k \rangle_{\text{local}}$ at fixed k . The normalized k NN spacings are then

$$s_n^k = \frac{\tilde{s}_n^k}{\langle \tilde{s}^k \rangle_{\text{local}}}, \quad \langle s^k \rangle_{\text{local}} \simeq 1. \quad (20)$$

This unfolding procedure is performed independently for each k . The corresponding probability density is denoted $P^k(s)$.

B. Nonoverlapping k -order gap ratios

As a complementary diagnostic that does not require unfolding, we compute the nonoverlapping k -order gap ratios

¹ Varying q in the range [20, 100] did not affect the inferred statistics.

$$r_n^k = \frac{\min(\tilde{s}_n^k, \tilde{s}_{n+k}^k)}{\max(\tilde{s}_n^k, \tilde{s}_{n+k}^k)} = \frac{\min(E_{n+k} - E_n, E_{n+2k} - E_{n+k})}{\max(E_{n+k} - E_n, E_{n+2k} - E_{n+k})}, \quad (21)$$

with $r_n^k \in [0, 1]$ and denote their distribution by $P^k(r)$.

In the sector with an odd total number of particles $N = N_\uparrow + N_\downarrow$, the spectrum contains exact doublets; consequently, the $k = 1$ spacing distribution includes a sharp accumulation at $s = 0$ and the nearest-neighbor ratio r_n^1 becomes identically zero for all n (and is therefore not informative). For this reason, and because we are interested in correlations between distinct doublets, we emphasize $k \geq 2$ spacing and ratio statistics, which probe correlations between distinct doublets rather than the trivial intra-doublet spacings for odd parity.

In the presence of exact degeneracies, we also compute a “collapsed” version of the spacing data in which exact degeneracies are removed before forming the level spacings,² leaving a set of nondegenerate eigenvalues. Unless explicitly stated otherwise, all reported spectral statistics and comparisons use the standard, noncollapsed spacings.

C. Reference RMT distributions and effective (k^*, β^*)

To compare with random-matrix theory (RMT) benchmarks, we use the generalized Wigner surmise for the k NN spacing distribution,

$$P^k(s, \beta) \approx C_\alpha s^\alpha \exp[-A_\alpha s^2], \quad (22)$$

where $\beta = 1, 2, 4$ is the Dyson index corresponding to GOE, GUE, and GSE, respectively. In this approximation, the exponent α is related to (β, k) by [11, 12]

$$\alpha(\beta, k) = \frac{k(k+1)}{2} \beta + k - 1. \quad (23)$$

The coefficients A_α and C_α are fixed by normalization and unit mean spacing: $\int_0^\infty P^k(s) ds = 1$ and $\int_0^\infty s P^k(s) ds = 1$, and thus equal to

$$A_\alpha = \left[\frac{\Gamma(\frac{\alpha}{2} + 1)}{\Gamma(\frac{\alpha+1}{2})} \right]^2, \quad C_\alpha = \frac{2 \Gamma^{\alpha+1}(\frac{\alpha}{2} + 1)}{\Gamma^{\alpha+2}(\frac{\alpha+1}{2})}. \quad (24)$$

The Wigner surmise (22) with the integer exponent α given by (23) does not reproduce the variance $\Delta_\beta^{(k)}$ of the level spacing distribution $P^k(s, \beta)$ which is known analytically and reads

$$\Delta_\beta^{(k)} = \frac{1}{k^2} \left(\frac{2 \ln k}{\pi^2 \beta} + c_\beta \right). \quad (25)$$

The constant c_β is the boundary condition, namely the variance for $k = 1$. The factor k^{-2} in the above equation appears due to our normalization $\langle s^k \rangle = 1$, which is different from the one in Ref. [13], namely $\langle s^k \rangle = k$. In Ref. [13] it is proposed to use for c_β the (inexact) variance given of the Wigner surmise (22)-(23), namely $c_1 = 4/\pi - 1$, $c_2 = 3\pi/8 - 1$, $c_4 = 45\pi/128 - 1$, and to choose the exponent α for $k \geq 2$ by imposing that the variance is given exactly by (25). This gives a noninteger exponent denoted by $\tilde{\alpha}(\beta, k)$, which is used in place of (23). It is found that this *new surmise* leads to a better approximation of the exact k NN level spacing distribution compared to (22)-(23).

The unfolded k NN level spacings computed numerically are fitted to Eq. (22), with α as the only free parameter, yielding α_{fit} . The effective ensemble Dyson index β^* and effective order k^* that best describe the observed distribution are chosen by minimizing $|\alpha_{\text{fit}} - \tilde{\alpha}(\beta, k)|$ over $\beta \in \{1, 2, 4\}$ and $k \leq 4$.

For gap ratios, we compare directly to RMT predictions without unfolding, using known analytical forms for the gap-ratio statistics at $k = 1$ [10, 15] and their higher-order generalizations [11, 12].

² In our implementation, eigenvalues closer than a tolerance factor of `frac` = 10^{-11} are treated as degenerate for the LSS calculation.

D. Multi-block spectra and m -block reference distributions

A common complication in spectral statistics analysis is the presence of multiple independent blocks that can arise from unresolved symmetries or Hilbert space fragmentation. If the spectrum is a superposition of m statistically independent blocks, levels from different blocks do not repel, and nearest-neighbor statistics can appear closer to a Poisson-like distribution, even when each block individually exhibits Wigner-Dyson correlations [16–19]. Higher-order diagnostics are particularly useful for resolving such hidden block structures [11, 20, 21].

Accordingly, in addition to single-block comparisons, we compare our data to multi-block reference distributions $P^k(s/r, \beta, m)$ obtained by superposing m independent RMT spectra drawn from the β -Gaussian ensemble. Throughout, m denotes the number of blocks, and we assume equal spectral densities for each block in the reference model, i.e., each block contributes equally many levels to the merged spectrum.

1. Monte Carlo generation of $P^k(s/r; \beta, m)$

Closed-form expressions for $P^k(s/r, \beta, m)$ are generally not available for arbitrary (k, β, m) . We therefore generate reference distributions by Monte Carlo sampling.

For each $\beta \in \{1, 2\}$, we generate independent RMT spectra using the Dumitriu-Edelman tridiagonal construction [22]. Specifically, we sample m independent β -ensemble matrices of dimension $N_{\text{RMT}} = 1000$ and compute their ordered eigenvalues. We then merge the m eigenvalue lists into a single ordered spectrum and compute k NN spacings and ratios from the merged list exactly as for the many-body data, including the unfolding procedure followed for $P^k(s)$. This procedure is performed $N_{\text{samp}} = 1000$ times, and the $P^k(s/r, \beta, m)$ distributions are computed for the combined data.

2. Choosing the closest (β, m) reference

To determine the best matching (β, m) for a given set of eigenvalues obtained from exact diagonalization, we compare the empirical distributions to the Monte Carlo reference distributions and select the closest match. We use two complementary metrics:

1. The Kolmogorov-Smirnov (KS) distance between empirical and reference cumulative distribution functions (CDFs) [23, 24].
2. A mean-square deviation (MSD) between empirical and reference distributions, evaluated on the histogram bins.

Let $\{x_{(i)}\}_{i=1}^N$ denote the sorted data values (either spacings or ratios), and define the empirical CDF evaluated at these points as

$$F_{\text{emp}}(x_{(i)}) = \frac{i}{N}. \quad (26)$$

For an analytic reference curve given as a probability distribution sampled on a grid, we construct the corresponding model CDF by trapezoidal integration and normalization, and then evaluate it at the data points by linear interpolation, yielding $F_{\text{model}}(x_{(i)})$. For Monte Carlo (m -block) references, we instead evaluate the reference CDF at the data points via

$$F_{\text{ref}}(x_{(i)}) = \frac{1}{N_{\text{ref}}} \# \{x_j^{\text{ref}} \leq x_{(i)}\}, \quad (27)$$

implemented by counting the number of reference samples that lie below each data point. In both cases, the Kolmogorov-Smirnov distance is then

$$D_{\text{KS}} = \max_{1 \leq i \leq N} |F_{\text{emp}}(x_{(i)}) - F_{\text{ref}/\text{model}}(x_{(i)})|. \quad (28)$$

For MSD, we work at the level of histogram densities. Let $\{b_j\}_{j=0}^B$ be the bin edges used for the empirical histogram (we use $B = 30$ bins over the relevant support interval). Writing h_j for the empirical density in bin j , and m_j for the corresponding model/reference density, we define

$$\text{MSD} = \frac{1}{B} \sum_{j=1}^B (h_j - m_j)^2. \quad (29)$$

For analytic (continuous) reference curves, m_j is obtained by numerically integrating the model probability distribution to form a normalized CDF on a fine grid, interpolating this CDF to the bin edges, and converting the resulting bin probabilities to densities by division by the bin widths. For Monte Carlo m -block references, m_j is obtained directly from a histogram of the reference samples evaluated on the same bin edges.

To establish a matching (β, m) pair, we require consistency across multiple diagnostics: agreement between $P^k(s)$ and $P^k(r)$, and stability across k values. In ambiguous cases, the gap-ratio statistics are preferred to the level-spacing statistics, as they do not require an unfolding procedure. The KS distance is the primary criterion for assigning the most likely number of blocks m , while MSD is a secondary tie-breaker. The effective ensemble index and order (β^*, k^*) are inferred from the level-spacing distribution via α_{fit} , and the same values are also used in the plots of the nonoverlapping gap ratio. The resulting labels (k^*, β^*) or $(k; \beta, m)$ are reported in all the figures and in Tab. I in the main text.

III. SUPPORTING RESULTS

A. Level spacing statistics of $\hat{\mathcal{H}}_{0,0}$

As shown in Fig. 1(d) in the main text, the spectrum of $\hat{\mathcal{H}}_{0,0} = \hat{\mathcal{H}}_{\text{tr}}$ is characterized by highly degenerate multiplets, which are the result of the presence of an extensive number of LIOMs, namely the operators \hat{S}_{nl}^2 discussed in Sec. I A. These degeneracies manifest in the level spacing distribution as a large peak at $s = 0$, as shown in Fig. 2. The level-spacing distribution of $\hat{\mathcal{H}}_{0,0}$ does not depend qualitatively on the particle number parity. Similar level-spacing distributions highly concentrated around zero are sometimes called “stick statistics” and are encountered in integrable systems built from commuting local projectors [25] and non-interacting systems, for instance spin chains that can be mapped to free fermions by the Jordan-Wigner transformation and collections of harmonic oscillators with commensurate frequencies [26–29].

To probe correlations between distinct many-body energies, we also show in Fig. 2 the level spacing distribution of the collapsed spectrum introduced in Sec. II B, namely the sequence of energy values obtained by replacing each degenerate multiplet with a single energy level. For $(\lambda_2, \lambda_3) = (0, 0)$, the resulting 1NN spacing and gap-ratio distributions are close to the Poisson benchmark, indicating that once the degeneracies are factored out, the remaining levels are likely uncorrelated [30, 31].

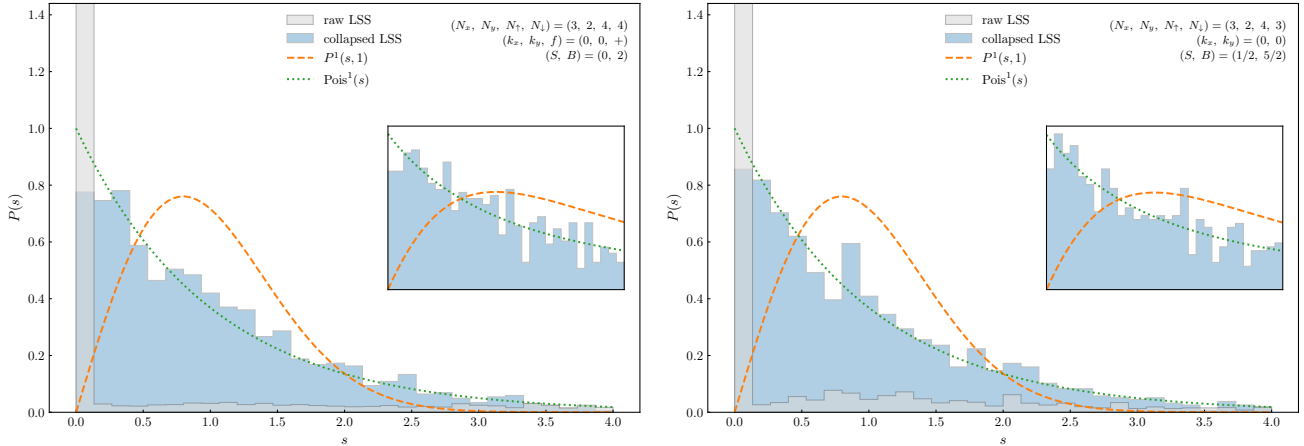


FIG. 2. Level spacing statistics for $\hat{\mathcal{H}}_{0,0}$ computed on both the raw level spacings and when all degeneracies are collapsed in the even- N sector (left) and odd- N sector (right). The raw level statistics exhibit a so-called “stick” structure, characterized by a dominant peak at $s = 0$. The collapsed spectrum exhibits level spacing statistics close to the Poisson distribution. The inset shows the gap ratio distribution for the collapsed spectrum, which also highlights the near-Poisson behavior.

B. Dependence of average gap ratio on λ_2 and λ_3

Fig. 3 shows the mean nonoverlapping gap ratios $\langle r^k \rangle$ across the (λ_2, λ_3) plane. Near $(\lambda_2, \lambda_3) = (0, 0)$, the spectrum is highly degenerate (consistent with the extensive LIOM structure of $\hat{\mathcal{H}}_{\text{tri}}$, see Fig. 2) and $\langle r^k \rangle$ is strongly suppressed

regardless of the parity. Turning on λ_2 or λ_3 lifts these degeneracies and leads to the increase of $\langle r^k \rangle$. Already for small nonzero λ_i , the mean nonoverlapping gap ratio displays a strong parity-dependent behavior: in the even-parity sector, $\langle r^k \rangle$ approaches values compatible with the ones expected for uncorrelated eigenvalues or a spectrum composed of several independent blocks. Moreover, the mean gap ratio increases monotonically with the order k , $\langle r^k \rangle < \langle r^{k+1} \rangle$. On the other hand, in the odd-parity sector, the 1NN mean gap ratio is identically zero due to the double degeneracy, and one observes the nonmonotonic behavior $\langle r^{(3)} \rangle < \langle r^{(2)} \rangle, \langle r^{(4)} \rangle$. Finally, both parities show a pronounced feature along $\lambda_2 = \lambda_3$, which is the condition for the total pseudospin B to be a good quantum number. Near this line, the total pseudospin symmetry is only approximate, and the associated reduction in level repulsion manifests as a decrease in the gap ratio. Exactly at $\lambda_2 = \lambda_3$, the pseudospin symmetry can be resolved in the numerics, leading to the discontinuity in the mean gap ratio visible in the figure since its value is close to the one attained in the region far from the diagonal.

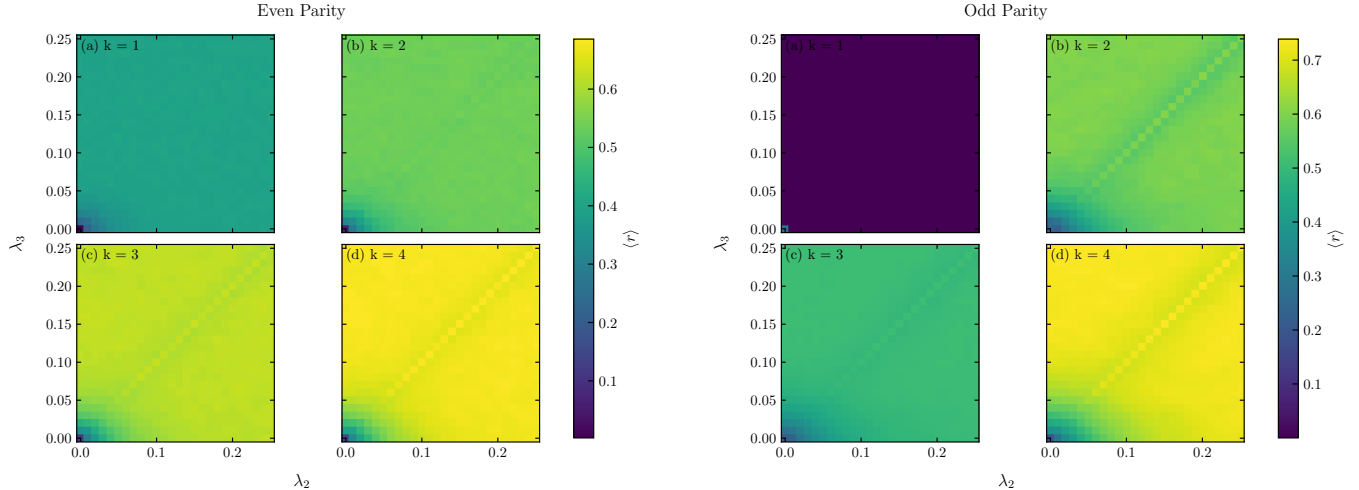


FIG. 3. (left): Mean k NN nonoverlapping gap ratio $\langle r^k \rangle$ of $\hat{\mathcal{H}}_{\lambda_2, \lambda_3}$ as a function of (λ_2, λ_3) for the even- N sector for lattice size $N_x = 3, N_y = 2$, with $k = 1, 2, 3, 4$ in panels (a), (b), (c) and (d), respectively. The point $(\lambda_2, \lambda_3) = (0, 0)$ corresponds to $\hat{\mathcal{H}}_{\text{tri.}}$, where the spectrum is highly degenerate and all $\langle r^k \rangle$ are strongly suppressed. Increasing λ_2 and/or λ_3 quickly lifts these degeneracies, and the mean gap ratio increases for any order k . (right): Same as (left) but for the odd- N sector. The 1NN ratio $\langle r^1 \rangle$ in panel (a) is exactly zero everywhere, reflecting the complete double degeneracy of the spectrum. For $k \geq 2$ the mean gap ratios increase with λ_2 and λ_3 , but in contrast to the even- N case, they are nonmonotonic in k : away from $(0, 0)$ we see that $\langle r^3 \rangle < \langle r^2 \rangle, \langle r^4 \rangle$. Note also the discontinuity of the mean gap ratio along the diagonal. This becomes more visible with increasing order k and is the result of the fact that only for $\lambda_2 = \lambda_3$ the pseudospin symmetry is exact and can be resolved in the numerics.

C. Local observables within degenerate doublets

Figure 4 shows the site-resolved total particle density $\rho_{n1,i} = \langle \psi_i | \hat{\rho}_{n1} | \psi_i \rangle$ and spin density $S_{n1,i}^z = \langle \psi_i | \hat{S}_{n1}^z | \psi_i \rangle$ for two orthonormal states $|\psi_{1,2}\rangle$ spanning a representative degenerate doublet in the odd-parity sector. An orbital exchange relates the two states: within each unit cell, $\rho_{n1,i}$ and $S_{n1,i}^z$ are mapped into each other by a flip of the Wannier index $n = 1 \leftrightarrow 2$, for instance $\rho_{1,1,1} = \rho_{2,1,2}$. This suggests that the states within each doublet are potentially related by a not-yet-identified symmetry that involves the Wannier/band degree of freedom. Choosing a different pair of orthonormal states as a basis for the same degenerate doublet leads to the same result shown in Fig. 4 with different specific values of $\rho_{n1,i}$ and $S_{n1,i}^z$. The same symmetry applies also to any degenerate doublet in the odd-parity sector.

D. Spectral statistics for different system sizes

Figs. 5–8 present the spectral statistics analysis for the different system sizes used to fill the entries of Tab. I in the main text. Fig. 5 and 6 show the level spacing and nonoverlapping gap ratio statistics for system size $N_x, N_y = 4, 2$ in the even- and odd-parity sectors, respectively. The results are very similar to the ones for size $N_x, N_y = 3, 2$ shown in the main text, with the only significant difference that for even particle number the best matching number of GOE

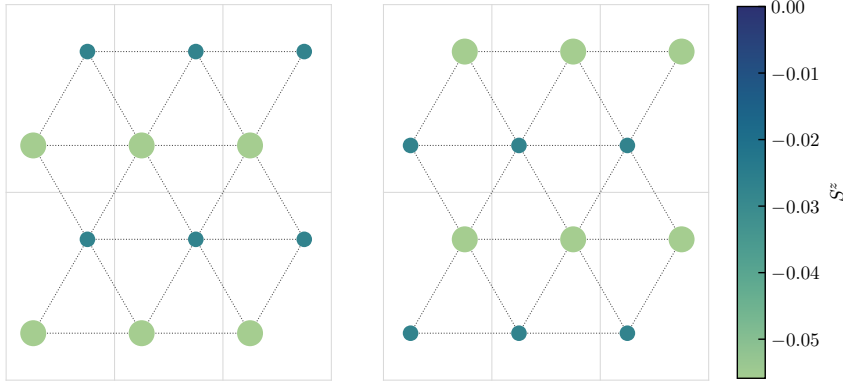


FIG. 4. Site-resolved total particle density $\rho_{nl,i} = \langle \psi_i | \hat{\rho}_{nl} | \psi_i \rangle$ and spin density $S_{nl,i}^z = \langle \psi_i | \hat{S}_{nl}^z | \psi_i \rangle$ for ψ_1 (left) and ψ_2 (right) calculated for $(N_x, N_y, N_\uparrow, N_\downarrow, k_x, k_y) = (3, 2, 2, 3, 0, 0)$. Here, $\psi_{1,2}$ are two orthonormal states spanning a selected degenerate doublet. The two markers within each rectangular unit cell correspond to the two Wannier orbitals ($n = 1, 2$). The diameter of the circle represents the relative particle density at a site, and the spin density is represented by the color scale. The values of $\rho_{nl,i}$ and $S_{nl,i}^z$ relative to the two states are mapped into each other by a flip in the Wannier index $n = 1 \leftrightarrow 2$.

blocks is $m = 6$ for size $N_x, N_y = 4, 2$ instead of $m = 4$. For odd parity, the match with the GUE distribution for $k = 2$ and $k = 4$ is excellent, as in the case of the data shown in the main text.

The largest system size accessible with exact diagonalization is $N_x, N_y = 3, 3$. The spectral statistics analysis for this system size is shown in Fig. 7 (even N) and Fig. 8 (odd N). For even parity, the spectral statistics is clearly compatible with the superposition of two GOE blocks. In the odd- N case, the particle number is limited to $N_\uparrow, N_\downarrow = 3, 2$, for which the dimension of the larger symmetry sector is relatively small, leading to relatively poor statistics compared to the other sizes. Moreover, we observe a pronounced peak at $s/r = 0$, indicating a large number of quasidegenerate states that appear for very low filling. This peak leads to poor fits to the Wigner surmise (22), as shown for instance in Fig. 8(d). Thus, only for this figure, the automatic procedure described in Secs. II C and II D used to identify the best matching numbers β^*, k^*, m is not used for the 2NN and 4NN distributions. Rather, we directly pick the GUE distributions with effective order $k^* = 1$ [panels (b) and (e) of Fig. 8] and $k^* = 2$ [panels (d) and (g)]. These match rather well the numerical data if the peak at $s/r = 0$ is ignored, as in the case of the other system sizes reported in Tab. I in the main text. For the future, it would be important to verify that the peak disappears and one obtains a better fit to the GUE distribution upon increasing the particle numbers while keeping the system size fixed. This can be done by using more sophisticated numerical methods that allow access to larger system sizes, as discussed in the main text.

Effect of a quadratic hopping term

To test the stability of the observed parity-dependent double degeneracy and spectral statistics, we add to $\hat{\mathcal{H}}_{1,1}$ a single-particle nearest-neighbor hopping term

$$\hat{\mathcal{H}}_t = -t \sum_{\langle nl, n'l' \rangle, \sigma} \left(\hat{d}_{nl\sigma}^\dagger \hat{d}_{n'l'\sigma} + \text{H.c.} \right), \quad (30)$$

which preserves translational invariance, SU(2) spin symmetry, spin-flip symmetry, and time-reversal symmetry, and conserves the total particle number, but breaks total pseudospin symmetry. This term lifts the exact double degeneracy for odd parity and removes the multi-block structure observed for even parity. The spectral statistics become essentially parity- and size-independent and are consistent with a single GOE block. This is expected for generic time-reversal and rotationally symmetric Hamiltonians after all symmetries have been resolved. For the results shown in the last column of Tab. I in the main text, we use $t = 0.1$ for the hopping amplitude.

[1] K. Swaminathan, P. Tadros, and S. Peotta, Signatures of many-body localization of quasiparticles in a flat band superconductor, *Physical Review Research* **5**, 043215 (2023).

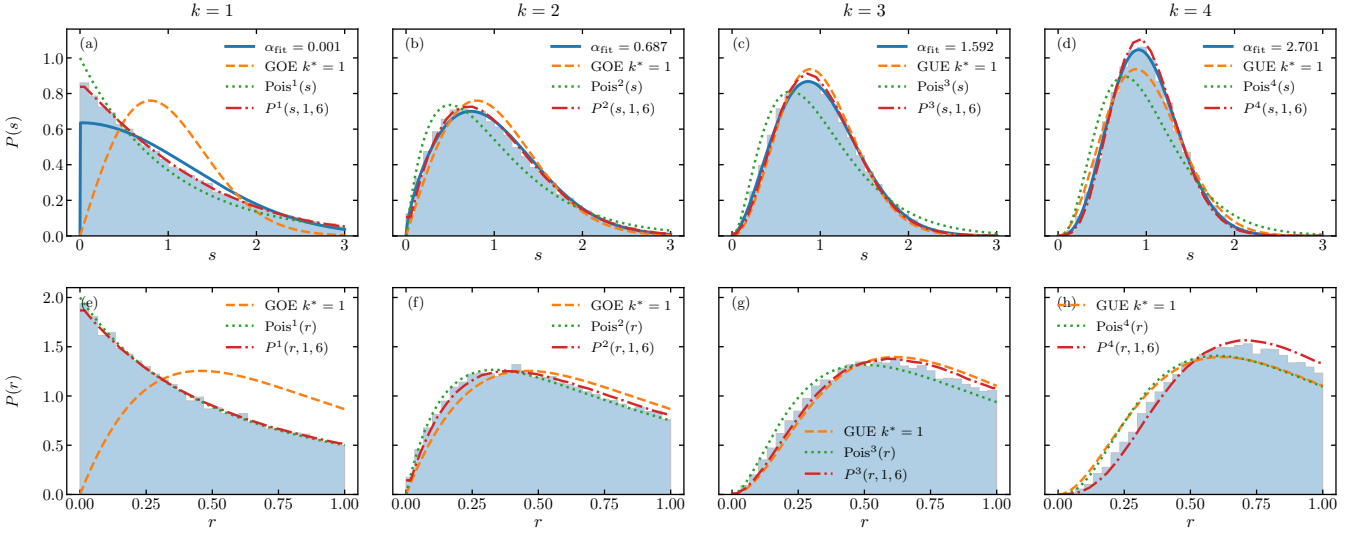


FIG. 5. Level spacing (top) and gap ratio (bottom) statistics of $\hat{\mathcal{H}}_{1,1}$ for even- N , size $N_x, N_y = 4, 2$, and quantum numbers $(N_\uparrow, N_\downarrow, k_x, k_y, S, B) = (6, 2, 0, 0, 2, 5)$ (Hilbert-space dimension $\mathcal{N} = 89652$). In the top row, the solid line shows the fit to (22). In both rows, the dashed curve is the closest matching Wigner surmise with effective order k^* (ensemble β^*). The dotted curve shows the k NN Poisson distribution, and the dash-dot curve is the closest matching m -block GOE distribution for each k . Both level spacing and gap ratio distributions are consistent with a superposition of $m = 6$ GOE blocks for any k .

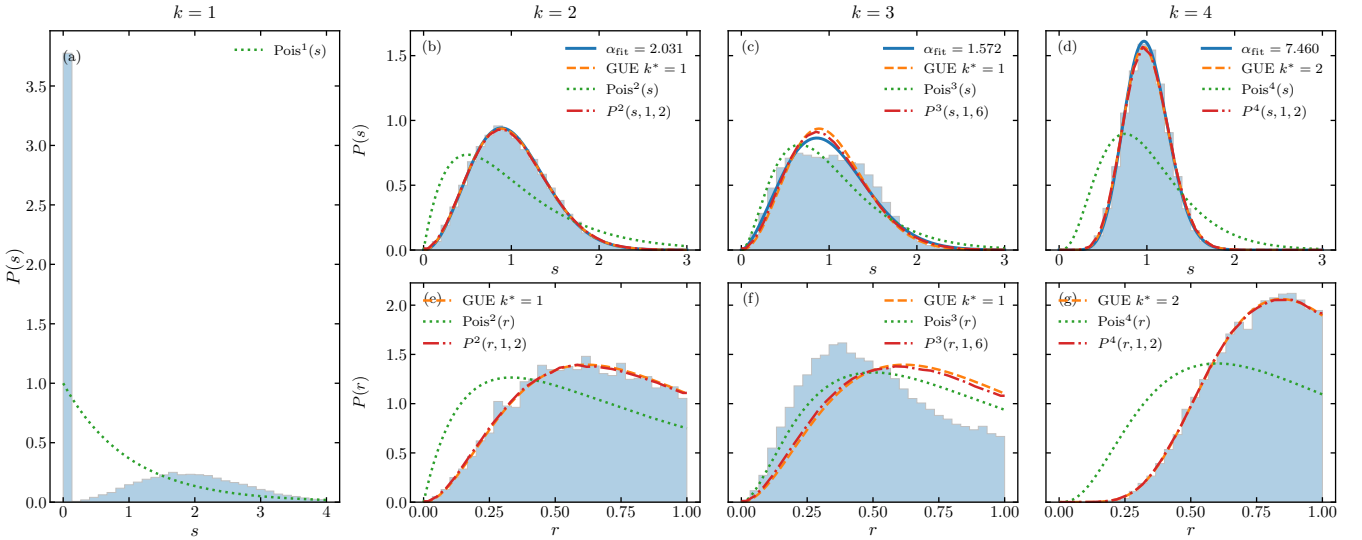


FIG. 6. Same as Fig. 5, but for odd- N and quantum numbers $(N_\uparrow, N_\downarrow, k_x, k_y, S, B) = (4, 3, 0, 0, 1/2, 9/2)$ (dimension $\mathcal{N} = 57120$). For $k = 1$, the double degeneracy leads to a pronounced peak at $s = 0$ in the level-spacing distribution and identically zero gap ratio (21) (not depicted). The $k = 2, 4$ statistics are well described by the GUE with $k^* = 1, 2$, equivalent to the superposition of two GOE blocks due to the known relation $P^{2k^*}(s/r, 1, 2) = P^{k^*}(s/r, 2)$. However, the $k = 3$ case clearly deviates from the superposition of two GOE blocks.

- [2] M. Tovmasyan, S. Peotta, L. Liang, P. Törmä, and S. D. Huber, Preformed pairs in flat Bloch bands, *Physical Review B* **98**, 134513 (2018).
- [3] S. M. Zhang and L. Jin, Compact localized states and localization dynamics in the dice lattice, *Physical Review B* **102**, 054301 (2020).
- [4] M. L. Mehta, *Random Matrices*, 3rd ed., Pure and Applied Mathematics, Vol. 142 (Academic Press, 2004).
- [5] D. Poilblanc, T. Ziman, J. Bellissard, F. Mila, and G. Montambaux, Poisson vs. GOE Statistics in Integrable and Non-Integrable Quantum Hamiltonians, *Europhysics Letters* **22**, 537 (1993).

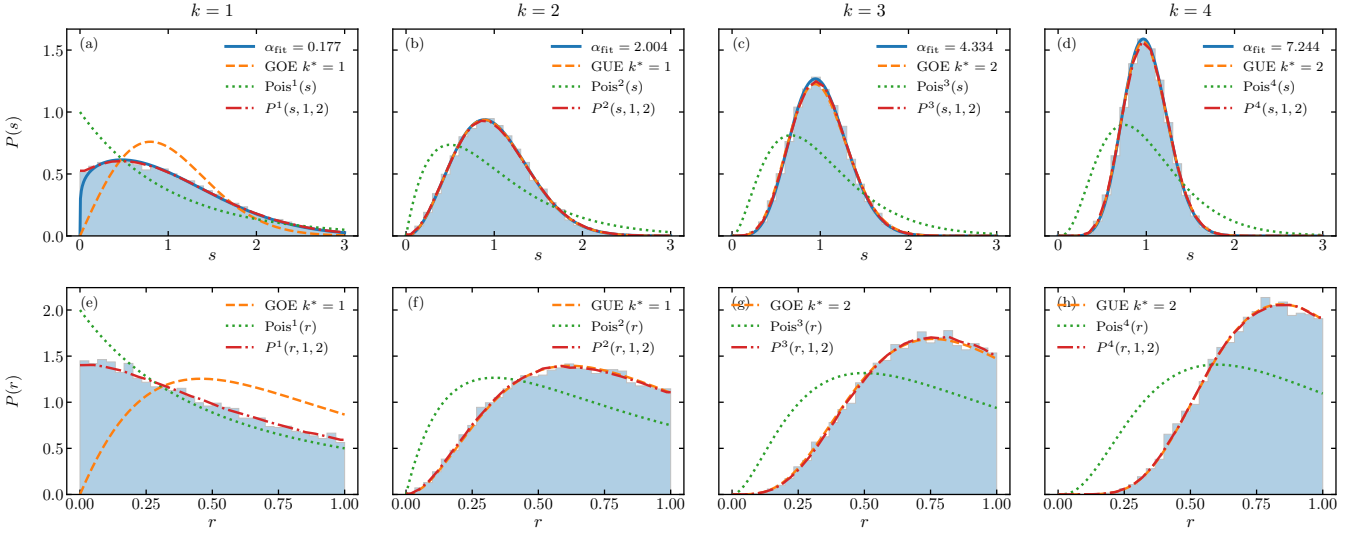


FIG. 7. Same as Fig. 5, but for size $N_x, N_y = 3, 3$ and quantum numbers $(N_\uparrow, N_\downarrow, k_x, k_y, f, S, B) = (3, 3, 0, 0, +, 1, 6)$ (dimension $\mathcal{N} = 33592$). Both level-spacing and gap-ratio distributions are consistent with the superposition of two GOE blocks for any k .

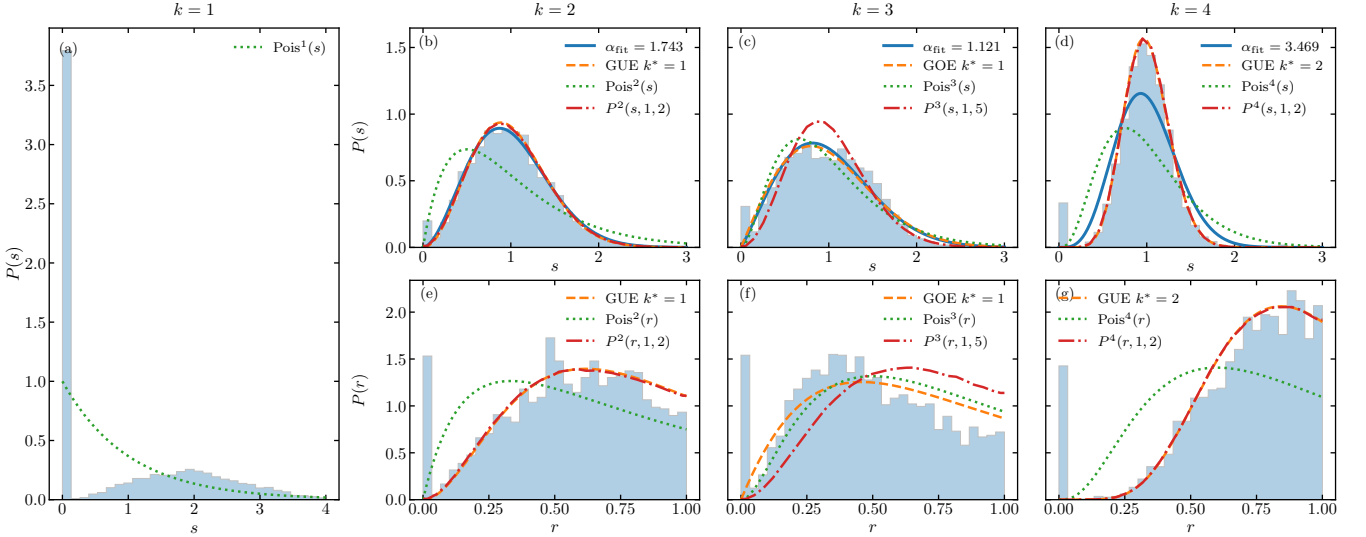


FIG. 8. Same as Fig. 5, but for size $N_x, N_y = 3, 3$, odd- N and quantum numbers $(N_\uparrow, N_\downarrow, k_x, k_y, S, B) = (3, 2, 0, 0, 1/2, 13/2)$ (dimension $\mathcal{N} = 7542$). For $k = 1$, the double degeneracy leads to a pronounced peak at $s = 0$ in the level spacing distribution and identically zero gap ratio (21) (not depicted). The $k = 2, 4$ statistics are well described by the GUE with $k^* = 1, 2$, equivalent to the superposition of two GOE blocks (if the large peak at $s/r = 0$ is ignored) due to the known relation $P^{2k^*}(s/r, 1, 2) = P^{k^*}(s/r, 2)$. However, the $k = 3$ case clearly deviates from the superposition of two GOE blocks.

- [6] M. Teeriaho, V.-V. Linho, K. Swaminathan, and S. Peotta, Coexistence of ergodic and nonergodic behavior and level spacing statistics in a one-dimensional model of a flat band superconductor, *Physical Review Research* **7**, 013318 (2025).
- [7] P. Weinberg and M. Bukov, QuSpin: A Python package for dynamics and exact diagonalisation of quantum many body systems part I: Spin chains, *SciPost Physics* **2**, 003 (2017).
- [8] P. Weinberg and M. Bukov, QuSpin: A Python package for dynamics and exact diagonalisation of quantum many body systems. Part II: Bosons, fermions and higher spins, *SciPost Physics* **7**, 020 (2019).
- [9] V. Oganesyan and D. A. Huse, Localization of interacting fermions at high temperature, *Physical Review B* **75**, 155111 (2007).
- [10] Y. Y. Atas, E. Bogomolny, O. Giraud, and G. Roux, Distribution of the Ratio of Consecutive Level Spacings in Random Matrix Ensembles, *Physical Review Letters* **110**, 084101 (2013).

- [11] S. H. Tekur, U. T. Bhosale, and M. S. Santhanam, Higher-order spacing ratios in random matrix theory and complex quantum systems, *Physical Review B* **98**, 104305 (2018).
- [12] W.-J. Rao, Higher-order level spacings in random matrix theory based on Wigner's conjecture, *Physical Review B* **102**, 054202 (2020).
- [13] R. Shir, P. Martinez-Azcona, and A. Chenu, Surmise for random matrices' level spacing distributions beyond nearest-neighbors, *Journal of Physics A: Mathematical and Theoretical* **58**, 445206 (2025).
- [14] L. F. Santos, Integrability of a disordered Heisenberg spin-1/2 chain, *Journal of Physics A: Mathematical and General* **37**, 4723 (2004).
- [15] Y. Y. Atas, E. Bogomolny, O. Giraud, P. Vivo, and E. Vivo, Joint probability densities of level spacing ratios in random matrices, *Journal of Physics A: Mathematical and Theoretical* **46**, 355204 (2013).
- [16] P. Bleher and A. R. Its, *Random Matrix Models and Their Applications*, Mathematical Sciences Research Institute Publications No. 40 (Cambridge university press, Cambridge, 2001).
- [17] G. W. Anderson, A. Guionnet, and O. Zeitouni, *An Introduction to Random Matrices*, 1st ed. (Cambridge University Press, 2009).
- [18] P. Deift and P. J. Forrester, eds., *Random Matrix Theory, Interacting Particle Systems, and Integrable Systems*, Mathematical Sciences Research Institute Publications No. 65 (Cambridge University Press, Cambridge, 2014).
- [19] O. Giraud, N. Macé, É. Vernier, and F. Alet, Probing Symmetries of Quantum Many-Body Systems through Gap Ratio Statistics, *Physical Review X* **12**, 011006 (2022).
- [20] S. H. Tekur and M. S. Santhanam, Symmetry deduction from spectral fluctuations in complex quantum systems, *Physical Review Research* **2**, 032063 (2020).
- [21] U. T. Bhosale, Superposition and higher-order spacing ratios in random matrix theory with application to complex systems, *Physical Review B* **104**, 054204 (2021).
- [22] I. Dumitriu and A. Edelman, Matrix models for beta ensembles, *Journal of Mathematical Physics* **43**, 5830 (2002).
- [23] F. J. Massey, The Kolmogorov-Smirnov Test for Goodness of Fit, *Journal of the American Statistical Association* **46**, 68 (1951).
- [24] M. A. Stephens, EDF Statistics for Goodness of Fit and Some Comparisons, *Journal of the American Statistical Association* **69**, 730 (1974).
- [25] A. Kapustin and L. Fidkowski, Local Commuting Projector Hamiltonians and the Quantum Hall Effect, *Communications in Mathematical Physics* **373**, 763 (2020).
- [26] M. V. Berry and M. Tabor, Level clustering in the regular spectrum, *Proceedings of the Royal Society of London. A. Mathematical and Physical Sciences* **356**, 375 (1977).
- [27] F. He, A. Hutsalyuk, G. Mussardo, and A. Stampiggi, *Statistical Signatures of Integrable and Non-Integrable Quantum Hamiltonians* (2025), arXiv:2510.02440 [cond-mat].
- [28] B. Chakrabarti, A. Biswas, V. K. B. Kota, K. Roy, and S. K. Haldar, Energy-level statistics of interacting trapped bosons, *Physical Review A* **86**, 013637 (2012).
- [29] A. D. Kerin, B. Dietz, and J. Brand, *Quartic level repulsion in a quantum chaotic three-body system without symplectic symmetry* (2025), arXiv:2510.06772 [cond-mat].
- [30] F. Haake, *Quantum Signatures of Chaos*, Springer Series in Synergetics, Vol. 54 (Springer Berlin Heidelberg, Berlin, Heidelberg, 2010).
- [31] T. Guhr, A. Müller-Groeling, and H. A. Weidenmüller, Random-matrix theories in quantum physics: Common concepts, *Physics Reports* **299**, 189 (1998).